Nonlinear dynamics of skyrmion strings

Volodymyr P. Kravchuk ![ORCID]*

Leibniz-Institut für Festkörper- und Werkstoffforschung, IFW Dresden, 01171 Dresden, Germany;
Institut für Theoretische Festkörperphysik, Karlsruher Institut für Technologie, 76131 Karlsruhe, Germany;
and Bogolyubov Institute for Theoretical Physics of the National Academy of Sciences of Ukraine, 03143 Kyiv, Ukraine

The skyrmion core, percolating the volume of the magnet, forms a skyrmion string—a topological Dirac-string-like object. Here we analyze the nonlinear dynamics of a skyrmion string in a low-energy regime by means of the collective variables approach, which we generalized for the case of strings. Using the perturbative method of multiple scales (both in space and time), we show that the weakly nonlinear dynamics of the translational mode propagating along the string is captured by the focusing-type nonlinear Schrödinger equation. As a result, the basic "planar-wave" solution, which has the form of a helix-shaped wave, experiences modulational instability. The latter leads to the formation of cnoidal waves. Both types of cnoidal waves, dn- and cn-waves, as well as the separatrix soliton solution, are confirmed by micromagnetic simulations. Beyond the class of traveling-wave solutions, we found Ma-breather propagating along the string. Finally, we proposed a generalized approach that enables one to describe the nonlinear dynamics of the modes of different symmetries, e.g., radially symmetrical or elliptical.

I. INTRODUCTION

Magnetic skyrmions [1–7] have traditionally been considered as two-dimensional topological solitons existing in magnetic films with Dzyaloshinskii-Moriya interaction (DMI). During the past decade there has been an explosive development in skyrmionics, which is due in part to the number of skyrmion properties that may be useful for application in spintronic devices, namely topological protection and controllability by electrical currents [8–10]. Although the first experimental observation of skyrmion lattices [11] implied the existence of skyrmion strings aligned along the applied magnetic field, the three-dimensional structure of skyrmions was not considered in most studies. However, recent advances in experimental techniques have enabled the real-space imaging of skyrmion strings in noncentrosymmetric bulk magnets [12–14]. A skyrmion string (tube) is a skyrmion core percolating the volume of the magnet; see Fig. 1(a). It is analogous to vortex filaments in superfluids [15,16], superconductors [17], and Bose-Einstein condensates [18]. Skyrmion strings carry an emergent magnetic field [19] that is the source of the topological Hall effect [20] experienced by the conducting electron; see Fig. 1(b). The skyrmion string-based realization of Dirac strings in condensed matter was discussed in Ref. [21]. Note that termination of the skyrmion string results in the creation of a Dirac monopole and antimonopole pair known as Bloch points [21–24].

A number of physical effects have already been established for skyrmion strings. It was shown that spin excitations can propagate along the string for a distance of tens of micrometers [25]. Thus, the strings can be considered as magnonic waveguides for information transfer [26]. The nucleation and annihilation of skyrmion strings can be effectively controlled by an external magnetic field [27], as well as by electrical current [28]. Skyrmion strings can be moved by the spin-polarized current applied perpendicularly to the string [29–32]. This current-induced dynamics has a threshold character caused by the effects of pinning on the impurities. The longitudinal current, however, leads to string instability [33]. Skyrmion strings can merge or unwind by means of Bloch points [23,34–36]. The position of the Bloch point along the string can be controlled by the current pulses, opening up a range of design concepts for future three-dimensional (3D) spintronic devices [28]. A bunch of skyrmion strings immersed into the conical phase can twist and create a braid superstructure [37]. It is worth mentioning that in addition to skyrmion strings, there are a number of other stringlike topological objects in magnets that are of interest from both fundamental and applied points of view, e.g., vortex strings [38–42] and screw dislocations [43].

The linear spin excitations propagating along skyrmion strings are well studied both theoretically [25,44,45] and experimentally [25]. Previously we also reported on finding a nonlinear solution in form of a solitary-wave propagating along a skyrmion string [45]. Here we report on a systematic study of the possible nonlinear low-energy string dynamics. To this end, we generalize the collective variables approach and obtain a Thiele-like equation for the string. Next, using the perturbative method of multiple scales [46,47], we demonstrate that for the case of low-amplitude dynamics, the string equation of motion is reduced to the focusing-type nonlinear Schrödinger equation (NLSE). Next, by means of full-scale micromagnetic simulations we found a number of well-known
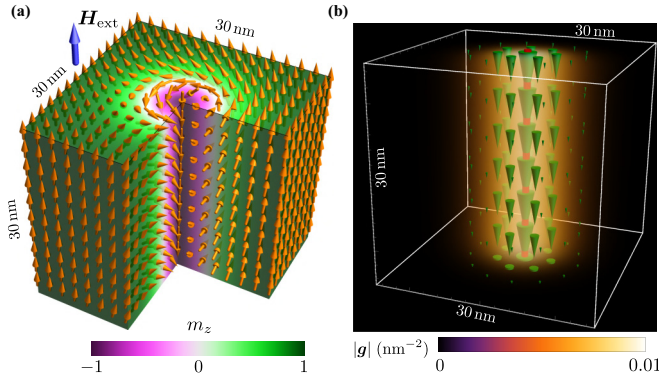
_____

*v.kravchuk@ifw-dresden.de

FIG. 1. Representation of a skyrmion string in terms of magnetization and the emergent magnetic field $\boldsymbol{B}^{e}$ [19] are shown in (a) and (b), respectively. In (a), arrows show the distribution of the magnetization $\boldsymbol{m}$, and color corresponds to the component m_z. In (b), arrows show the distribution of $\boldsymbol{B}^{e} \propto \boldsymbol{g}$ with $|\boldsymbol{B}^{e}|$ reflected by the color intensity; see Eq. (2). The central red line shows the position of the string center defined in (1). The data are obtained by means of micromagnetic simulations for FeGe in an external field, $\mu_0 H_{\text{ext}} = 0.8$ T.

solutions of the NLSE, namely nonlinear cnoidal waves, solitons, and breathers. These numerically found solutions agree very well with the predictions of our model. Finally, we suggest a generalization of the collective variables approach used for stringlike collective variables.

II. DEFINITION OF A SKYRMION STRING AND ITS EQUATION OF MOTION

We consider a cubic chiral ferromagnet saturated by an external magnetic field along the z-axis. Such a magnet can host a magnetic skyrmion as an excitation of the uniform ground state $\boldsymbol{m}(\boldsymbol{r}) = \hat{z}$ [48,49]. Here and below, the unit vector $\boldsymbol{m}$ denotes dimensionless magnetization. In the case of a bulk sample, the skyrmion core penetrates the magnet volume forming a stringlike object. In equilibrium, the string is oriented along $\hat{z}$. Deviation of the string shape from the equilibrium straight line results in the string dynamics. Our aim here is to describe this dynamics in the low-amplitude limit.

We define the skyrmion string as a time-dependent 3D curve $\boldsymbol{\gamma}(z, t) = \hat{x}X_1(z, t) + \hat{y}X_2(z, t) + z\hat{z}$, where

$$X_i(z, t) = \frac{1}{N_{\text{top}}} \iint x_i g_z(\boldsymbol{r}, t) dx dy \quad (1)$$

are the first moments of the topological charge density $g_z = \frac{1}{4\pi} \boldsymbol{m} \cdot [\partial_x \boldsymbol{m} \times \partial_y \boldsymbol{m}]$. Here $x_1 = x$ and $x_2 = y$. The total topological charge $N_{\text{top}} = \iint g_z dx dy$ is a constant integer number. Since the magnetization evolution is assumed to be continuous in space and time, and the boundary conditions $\boldsymbol{m} = \hat{z}$ are fixed for $\varrho = \sqrt{x^2 + y^2} \to \infty$, the topological charge N_{top} does not depend either on time or on the z coordinate. Note that g_z is a vertical (along the ground state) component of the gyrovector density

$$\boldsymbol{g} = \frac{\boldsymbol{e}_i \epsilon_{ijk}}{8\pi} \boldsymbol{m} \cdot [\partial_j \boldsymbol{m} \times \partial_k \boldsymbol{m}] \quad (2)$$

which determines the emergent magnetic field $\boldsymbol{B}^{e} \propto \boldsymbol{g}$ [19].

We base our study on the Landau-Lifshitz equation $\partial_t \boldsymbol{m} = \frac{\gamma_0}{M_s}[\boldsymbol{m} \times \frac{\delta H}{\delta \boldsymbol{m}}]$, which equivalently can be written in the Hamiltonian form $\partial_t \boldsymbol{m} = \{\boldsymbol{m}, H\}$ Supplemented with the Poisson brackets for the magnetization components

$$\{m_i(\boldsymbol{r}), m_j(\boldsymbol{r}')\} = -\frac{\gamma_0}{M_s} \epsilon_{ijk} m_k(\boldsymbol{r}) \delta(\boldsymbol{r} - \boldsymbol{r}'). \quad (3)$$

Here H is the Hamiltonian, γ_0 is the gyromagnetic ratio, and M_s is the saturation magnetization. Using (3) and definition (1), we obtain

$$\{X_i(z), X_j(z')\} = -\epsilon_{ij} \frac{\gamma_0}{M_s} \frac{\delta(z - z')}{4\pi N_{\text{top}}}; \quad (4)$$

for details, see Appendix A. This is a generalization of the previously obtained Poisson brackets for coordinates of 2D topological solitons [50]. In the following, we restrict ourselves by the low-energy limit and therefore we take into account only the collective variables X_1 and X_2, which are associated with the low-energy translation mode. In this case, the string equations of motion are $\partial_t X_i = \{X_i, H\}$. By means of (4) we obtain the following explicit form for the equations of motion: $\partial_t X_i = -\epsilon_{ij} G^{-1} \delta H / \delta X_j$, where $G = 4\pi N_{\text{top}} M_s / \gamma_0$ and $H = \int \mathcal{H}(\partial_z X_i, \partial_z^2 X_i, \dots) dz$. Note that due to the transnational invariance, the longitudinal Hamiltonian density $\mathcal{H}$ does not depend on X_i but only on its derivatives. For a number of problems, it can be convenient to introduce the vector $\boldsymbol{X} = X_1 \hat{x} + X_2 \hat{y}$. The corresponding equations of motion have the Thiele-like form [39,40,45] $[\partial_t \boldsymbol{X} \times \boldsymbol{G}] = \delta H / \delta \boldsymbol{X}$, where $\boldsymbol{G} = G\hat{z}$ is the string gyrovector. In contrast to the conventional Thiele equation [51], (i) the skyrmion position $\boldsymbol{X}(z, t)$ depends not only on time but also on the coordinate z, and (ii) the right-hand side of the equation of motion contains a functional derivative instead of the partial one.

In what follows, however, we use the alternative representation by means of the complex-valued function $\Psi = X_1 + iX_2$. The corresponding equation of motion is of the Schrödinger-like form

$$i\partial_t \Psi = -\frac{2}{G} \frac{\delta H}{\delta \Psi^*}. \quad (5)$$

Although the general form of the equation of motion (5) enables one to make a conclusion about some integrals of motion, e.g., total energy $E = H$ or linear momentum $P = G\frac{i}{4} \int (\Psi \partial_z \Psi^* - \Psi^* \partial_z \Psi) dz$, in order to obtain a concrete solution one needs to know the structure of the Hamiltonian $H = \int \mathcal{H} dz$. The concrete dependence of the effective Hamiltonian density $\mathcal{H}(\partial_z \Psi, \partial_z \Psi^*, \partial_z^2 \Psi, \dots)$ on the collective string-variable Ψ is determined by the magnetic interactions present in the system. In the following, we consider the case of a cubic chiral ferromagnet (e.g., FeGe, MnSi, Cu_2OSeO_3) immersed in an external magnetic field $\boldsymbol{H}_{\text{ext}} = H_{\text{ext}}\hat{z}$. The corresponding Hamiltonian

$$H = \int (A\mathcal{H}_{\text{ex}} + D\mathcal{H}_{\text{DMI}} + \mu_0 H_{\text{ext}} M_s \mathcal{H}_z) d\boldsymbol{r} \quad (6)$$

collects three contributions, namely the exchange energy with $\mathcal{H}_{\text{ex}} = \partial_i \boldsymbol{m} \cdot \partial_i \boldsymbol{m}$, where $i = x, y, z$, the

Dzyaloshinskii-Moriya energy with $\mathscr{H}_{DMI} = \boldsymbol{m} \cdot [\nabla \times \boldsymbol{m}]$, and the Zeeman energy with $\mathscr{H}_z = 1 - m_z$.

Typical length- and timescales of the system (6) are determined by the wave vector $Q = D/(2A)$ and frequency $\omega_{c2} = \gamma_0 D^2/(2AM_s)$, respectively. In terms of the dimensionless units $\tilde{\boldsymbol{r}} = \boldsymbol{r}Q$ and $\tilde{t} = t\omega_{c2}$, system (6) is controlled by a single parameter, which is the dimensionless magnetic field $h = H_{ext}/H_{c2}$, where $\mu_0 H_{c2} = \omega_{c2}/\gamma_0$. In the following, we consider the regime $H_{ext} > H_{c2}$ in which the ground state is uniformly polarized along the field. Such a polarized magnet can host isolated skyrmion strings as topologically protected excitations [45]. In the following, we proceed to the dimensionless order parameter $\psi = \Psi Q$.

Here we discuss two ways to derive the structure of the string Hamiltonian. The simplest way is based on the gradient expansion of the Hamiltonian density with respect to ψ, ψ^* and their derivatives. In the expansion, we keep only real-valued terms, which are not total derivatives with respect to z and which do not violate the translational and $U(1)$ symmetries. Due to the translational symmetry, the expansion terms can depend only on derivatives $\psi^{(n)}$ and $\psi^{*(m)}$, with $n, m = 1, 2, \ldots$. The $U(1)$ symmetry is a consequence of the isotropy of the model (6) within the xy-plane. As a result, the string Hamiltonian must be invariant with respect to the arbitrary rotations within the xy-plane, i.e., with respect to the replacement $\psi \to e^{i\alpha}\psi$. The latter implies that the only quadratic blocks $\psi^{(n)}\psi^{*(m)}$ are allowed in the string Hamiltonian expansion. This means that only even terms are allowed in the expansion, i.e., the leading nonlinear terms are of the fourth order. Finally, we present the string Hamiltonian as follows:

$$\tilde{H} = \int d\tilde{z}[\mathscr{H}^{(0)} + \mathscr{H}^{(2)} + \mathscr{H}^{(4)} + \cdots], \qquad (7)$$

where $\tilde{H} = H/(8\pi A Q^{-1})$ and $\tilde{z} = zQ$. Here $\mathscr{H}^{(0)}$ is the longitudinal energy density of the vertical unperturbed string; it does not depend on the collective string variable ψ. The harmonic and the leading nonlinear terms are as follows:

$$\mathscr{H}^{(2)} = \frac{a_1}{2}|\psi'|^2 + i\sigma\frac{a_2}{4}(\psi'\psi^{*''} - \psi^{*'}\psi'') + \frac{a_3}{2}|\psi''|^2$$
$$+ \cdots,$$
$$\mathscr{H}^{(4)} = -\frac{b_1}{4}|\psi'|^4 - i\sigma\frac{b_2}{8}|\psi'|^2(\psi'\psi^{*''} - \psi^{*'}\psi'') + \cdots,$$
$$(8)$$

where a prime denotes the derivative with respect to $\tilde{z}$. The terms proportional to $(\psi'\psi^{*''} - \psi^{*'}\psi'')$ are responsible for the nonreciprocal effects since they are not invariant with respect to the transformation $\tilde{z} \to -\tilde{z}$. Since the presence of the derivatives $\partial_{\tilde{z}}$ in DMI is the only source of nonreciprocity in the initial model (6), the nonreciprocal terms in (8) are proportional to $\sigma = \mathrm{sgn}(D) = \pm 1$. Note, however, that DMI is not the only contributor to the nonreciprocity coefficients a_2 and b_2. As will be shown latter (see Appendix D), the exchange and Zeeman interactions also contribute due to the helicity $\varphi_0 = \pm\pi/2$ of the Bloch skyrmion, such that $\sigma = \sin\varphi_0$. Indeed, due to the particular circulation of magnetization of the Bloch skyrmion string (clockwise or counterclockwise),
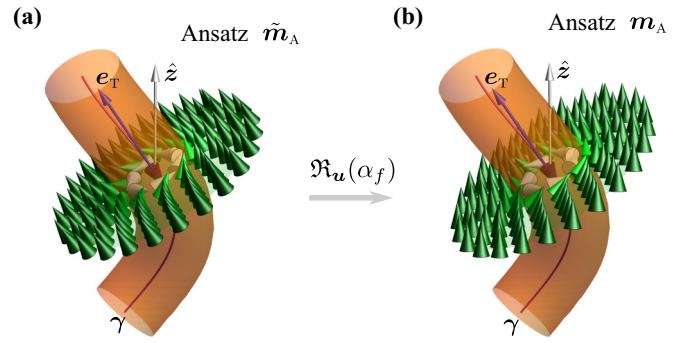

FIG. 2. Two-step formation of the skyrmion string ansatz. Models (C1) and (C2) are shown in (a) and (b), respectively. For ansatz $\tilde{\boldsymbol{m}}_A$, magnetization within a perpendicular cross section (shown by cones) coincides with the equilibrium 2D skyrmion solution. In ansatz $\boldsymbol{m}_A$, the magnetization within each cross section is inhomogeneously rotated such that $\boldsymbol{m}_A$ meets the ground state at a distance from the string; see Appendix C for details.

the directions $\pm\hat{z}$ arenot equivalent. For a Néel skyrmion string, the nonreciprocal terms are absent in the string Hamiltonian.

The second way to derive the structure of the string Hamiltonian is based on the skyrmion string ansatz, which is explained in detail in Appendix C. The string ansatz is built as a two-step deformation of the magnetization field $\boldsymbol{m}_0(x, y)$ of the unperturbed vertical string in equilibrium. In the first step, we consider a model $\tilde{\boldsymbol{m}}_A(\boldsymbol{r})$, such that the magnetization within each cross section perpendicular to the string coincides with $\boldsymbol{m}_0$ (in the reference frame, defined on the section plane); see Fig. 2(a). Although the model $\tilde{\boldsymbol{m}}_A$ is intuitively clear, it cannot be used because $\tilde{\boldsymbol{m}}_A$ is not uniquely defined if the distance to the string is larger than the curvature radius, and also $\tilde{\boldsymbol{m}}_A$ does not meet the ground state at large distances. For these reasons, in the second step, we apply a spatially dependent rotational transformation $\boldsymbol{m}_A = \mathfrak{R}_{\boldsymbol{u}}(\alpha_f)\tilde{\boldsymbol{m}}_A$ within each perpendicular cross section. The rotation is performed around the unit vector $\boldsymbol{u} = \boldsymbol{e}_T \times \hat{z}/|\boldsymbol{e}_T \times \hat{z}|$, where $\boldsymbol{e}_T$ is the unit vector, tangential to the string. The rotation magnitude α_f depends on the distance ρ to the string center (within each cross section), and it is such that $\alpha_f \to \angle(\boldsymbol{e}_T, \hat{z})$ everywhere except the small region $\rho < \rho^*$ around the string. Here $\rho^*\kappa \ll 1$, with κ being the string curvature. It is assumed that the angle α_f depends only on ρ. This dependence is captured by some unknown function $0 < f(\rho) < 1$ such that $\alpha_{f=0} = 0$ and $\alpha_{f=1} = \angle(\boldsymbol{e}_T, \hat{z})$; for details, see Appendix C. The resulting magnetization is shown in Fig. 2(b).

The localization area of function $f(\rho)$ determines the string vicinity whose magnetization is disturbed by the string deformation. Numerical computation of $f(\rho)$ shows that this area can exceed several times the skyrmion core radius; see Fig. 13 and the corresponding discussion in Appendix D. Another interesting observation is that $0 < f(0) < 1$, meaning that the magnetization on the string's central line $\boldsymbol{\gamma}$ is neither tangential to $\boldsymbol{\gamma}$ nor collinear to the applied magnetic field. However, $f(0) \to 1$ in the limit of large fields, i.e., the magnetization of the string line tends to be antiparallel to the field in this limit; see Appendix D.

The substitution of the string ansatz $\boldsymbol{m}_A$ into the Hamiltonian (6) and the integration over the coordinates perpendicular to the string enable us to write the string Hamiltonian in the form (7) and (8); for details, see Appendix D. The coefficients a_n and b_n are functionals of the skyrmion profile $\theta_0(\rho)$ and function $f(\rho)$. A rough estimation for the function $f(\rho)$ is discussed in Appendix D and is shown in Fig. 13. For details and the explicit form of the coefficients a_n and b_n, see Appendix D. Remarkably, the Hamiltonian obtained by means of the ansatz completely satisfies the symmetry requirements discussed above. Although the proposed model enables one to estimate coefficients a_n and b_n in a self-consistent manner, the numerical values of these coefficients can be obtained more accurately by means of micromagnetic simulations, as explained in Sec. III and Appendix F. The main simplification of the ansatz $\boldsymbol{m}_A$ is that the function $f(\rho)$ is assumed to be radially symmetric, i.e., it depends only on the radial distance (within a cross section) and not on the azimuth direction. As a result, the theoretically predicted values of a_n and b_n are somewhat larger than the numerically obtained ones; see Fig. 14 and the corresponding discussion in Appendix D.

In the limit of large magnetic fields (infinitely thin strings), one has $\mathscr{H}^{(2)} \approx \frac{1}{2}|\psi'|^2$ and $\mathscr{H}^{(4)} \approx -\frac{1}{8}|\psi'|^4$; see Appendix D. This reflects the increase of the string energy due to the increase of the total string length $\int \sqrt{1+|\psi'|^2}d\tilde{z}$, since $\sqrt{1+|\psi'|^2} \approx 1 + \frac{1}{2}|\psi'|^2 - \frac{1}{8}|\psi'|^4$. In this limit, the exchange contribution to the string energy dominates.

In dimensionless units, the equation of motion (5) reads $\frac{i}{2}\dot{\psi} = \frac{\delta\tilde{H}}{\delta\psi^*}$, where the overdot indicates the derivative with respect to dimensionless time $\tilde{t}$, and we took into account that $N_{\text{top}} = -1$. With (7) and (8), we write this equation of motion in the following explicit form:

$$-i\dot{\psi} = a_1\psi'' - ia_2\sigma\psi''' - a_3\psi^{(\text{IV})} + \cdots$$
$$- b_1(\psi'^2\psi^{*'})' + ib_2\sigma(\psi'\psi''\psi^{*'})' + \cdots . \quad (9)$$

The limit case of Eq. (9) with $a_{n>1} = 0$ and $b_{n>1} = 0$ was previously obtained and discussed in Ref. [45].

III. HELICAL WAVE

In spite of a complicated general form, Eq. (9) has a simple exact solution in the form of a nonlinear helical wave,

$$\psi = \mathcal{R}e^{i(k\tilde{z}-\omega\tilde{t})}, \quad (10)$$

where the real constant $\mathcal{R}$ plays the role of the helix radius. The helical wave (10) has the following dispersion relation:

$$\omega = \omega_0(k) - \mathcal{R}^2k^2\omega_1(k) + \cdots , \quad (11a)$$

$$\omega_0(k) = a_1k^2 + a_2\sigma k^3 + a_3k^4 + \cdots , \quad (11b)$$

$$\omega_1(k) = b_1k^2 + b_2\sigma k^3 + \cdots . \quad (11c)$$

In the limit $\mathcal{R} \to 0$, the helical wave is transformed into the translational magnon mode with the dispersion $\omega_0(k)$ shown in Fig. 3(a). For finite $\mathcal{R}$, the leading nonlinear term in the dispersion is represented by $\omega_1(k)$. The known forms of dispersions $\omega_0(k)$ and $\omega_1(k)$ enable one to determine coefficients a_n and b_n by means of numerical simulations of the helical wave dynamics for various $\mathcal{R}$ and k; for details, see Appendix F. The dependencies of several first coefficients a_n and
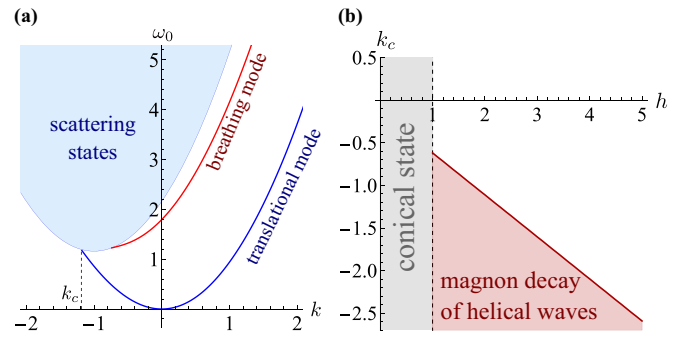

FIG. 3. (a) Dispersion relation for the translational and breathing linear modes propagating along the string in the field $h = 2.16$ ($\mu_0 H_{\text{ext}} = 0.8$ T) and for the case $\sigma > 0$. The data are obtained by means of diagonalization of the spin-wave Hamiltonian as explained in Ref. [45]. For $k < k_c$, the localized translational mode does not exist. The dependence of the critical wave vector k_c on the applied magnetic field is shown in (b). Helical waves (10) exist for $k > k_c$ only.

b_n on the applied magnetic field are shown in Fig. 4. Note that the normalized magnetic field h is the only parameter that controls system (6). We should emphasize that the numerical values of the coefficients a_n and b_n presented in Fig. 4 are universal and valid for all cubic chiral magnets.

The wave vector k of the helical wave (10) cannot be arbitrary. It is limited by the domain of existence of the localized translational magnon mode propagating along the string, i.e., $k > k_c(h)$; see Fig. 3. For the case $k < k_c$, the stationary helical wave (10) does not exist. In this regime, the helix radius $\mathcal{R}$ decays rapidly. This process is accompanied by the magnon emission. The regime of the magnon decay of the helical wave is shown in Fig. 3(b) by the red shading.

The restriction to the low-energy segment of the spectrum is supported by the gapless nature of the translational mode; see Fig. 3(a). In other words, in the long-wave regime, the translational mode is guaranteed to be energetically distant from the other modes which are gapped. However, this simplification can be violated in the close vicinity of the saturation field ($h = 1$), where the elliptic mode becomes also gapless
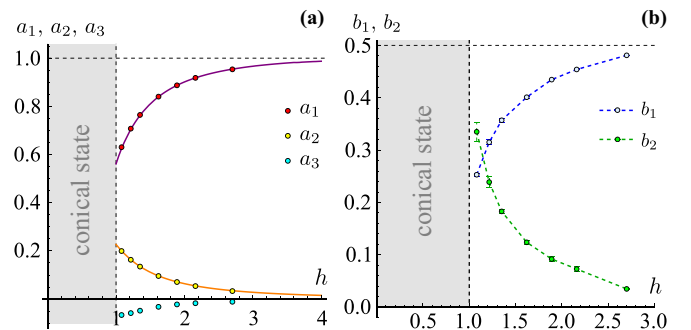

FIG. 4. The field dependence of the linear a_n and nonlinear b_n coefficients in the dispersion relation (11). Markers show the coefficient values obtained by means of numerical simulations; for details, see Appendix F. Solid lines show the dependencies of $a_1(h)$ and $a_2(h)$ previously extracted from the dispersion of the translational magnon mode; see Fig. 3(a) and Ref. [45] for details.
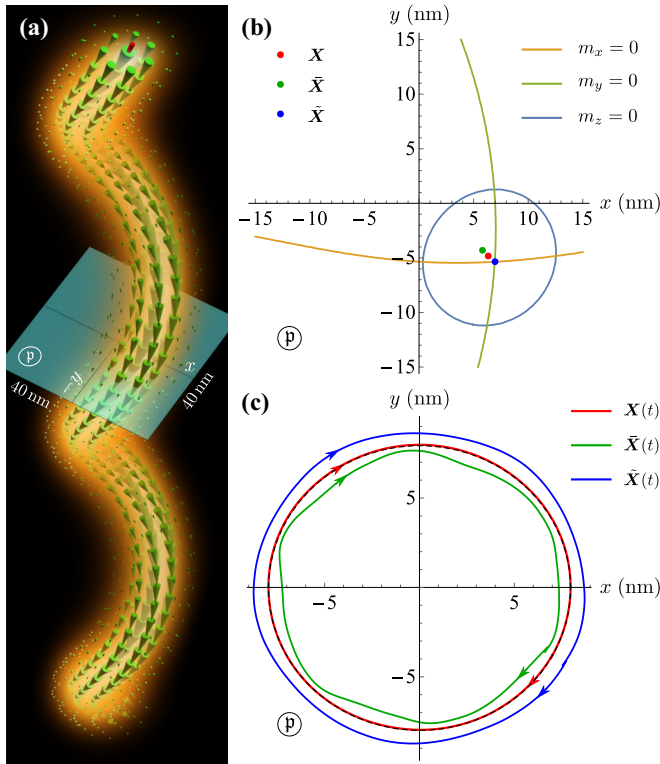
FIG. 5. (a) A snapshot of a helical wave propagating along a skyrmion string is shown in terms of the emergent field $\boldsymbol{B}^e$. Notations are the same as in Fig. 1(b). The helix radius and pitch are 8 and 120 nm ($k > 0$), respectively. Data are obtained from the micromagnetic simulations for FeGe (see Appendix E for details) in field $\mu_0 H_{ext} = 0.7$ T. (b) Magnetization isolines within the horizontal cross section by the plane ꝑ. Dots represent the cross sections with the string central lines defined in a different manner (explained in the text). The time evolution of these markers is shown in (c). The black dashed line shows the geometrical circle of radius 8 nm. The clockwise direction of motion along the trajectories takes place also for $k < 0$. The helical wave dynamics for both signs of k is illustrated by Supplemental movies 1 and 2 [57].

[52,53] and may influence the dynamics of the translational mode considered here.

Based on dispersions (11b) and (11c), and on the numerically obtained dependencies $a_n(h)$ and $b_n(h)$, we found that the Lighthill criterion [54,55]

$$\omega_0''(k)\omega_1(k) > 0 \qquad (12)$$

is satisfied for $k > k_c$ [56], meaning the modulational instability of the nonlinear helical wave (10). This effect and its consequences are discussed in the next section.

An example of the skyrmion filament with the propagating helical wave is shown in Fig. 5(a) in terms of the emergent magnetic field. A specificity of the preparation of the initial magnetization distribution used for the simulations (see Appendix F) is such that we can control the helix shape (10) of the central line defined in (1), however the overall magnetization structure $\boldsymbol{m}(\boldsymbol{r})$ can deviate slightly from the real solution determined by the Landau-Lifshitz equation. As a result, a number of higher skyrmion modes, e.g., a breathing or CCW mode, are excited together with the helical wave. These modes

are very well recognizable in the Supplemental movies 1 and 2 [57]. We use the presence of the additional magnon excitations in order to compare different definitions of the string central line alternative to (1). We consider two alternative definitions of the skyrmion guiding center which are the most common in the literature, namely the first moment of m_z component,

$$\bar{X}_i(z,t) = \frac{\iint x_i[1 - m_z(x,y,z,t)]dxdy}{\iint [1 - m_z(x,y,z,t)]dxdy}, \qquad (13)$$

and $\tilde{X}_i$: $m_z(\tilde{X}_1, \tilde{X}_2) = -1$. A comparison of different types of dynamics of the skyrmion guide-centers defined as (1) and (13) is discussed in a number of previous works [58–60], in which it was shown that the guiding center (1) demonstrates the massless Thiele dynamics, while the guiding center defined in (13) shows the additional oscillations typical for a massive particle. The definition $\tilde{X}_i$ was widely used to study the dynamics of merons [61–63], and it was shown that the guiding center $\tilde{\boldsymbol{X}}$ also demonstrates a complicated dynamics with several additional high-frequency oscillations such that the massive and the higher-order terms are required in the corresponding equation of motion for $\tilde{\boldsymbol{X}}(t)$ [61,64]. Here, using the helical wave as an example, we demonstrate that the string definitions $\boldsymbol{X}(z,t)$, $\bar{\boldsymbol{X}}(z,t)$, and $\tilde{\boldsymbol{X}}(z,t)$ are different; see Figs. 5(b) and 5(c). It is important that within an arbitrary horizontal cross section $z = z_0$, the trajectory $\boldsymbol{X}(z_0,t)$ is a circle, while trajectories $\bar{\boldsymbol{X}}(z_0,t)$ and $\tilde{\boldsymbol{X}}(z_0,t)$ exhibit additional cycloidal oscillations; see Fig. 5(c). This is in agreement with the results discussed above for two-dimensional topological solitons. The circular trajectory for $\boldsymbol{X}(z_0,t)$ is consistent with the helix solution (10), and this justifies *a posteriori* the initial massless equation (5), in which we implicitly assumed vanishing of the Poisson brackets of X_i with the amplitudes of higher magnon modes. However, as follows from Fig. 5(c), this assumption cannot be applied for strings $\bar{\boldsymbol{X}}(z,t)$ and $\tilde{\boldsymbol{X}}(z,t)$. From Fig. 5(c) one can conclude that the nonlinear interaction between the translational mode defined via $\boldsymbol{X}(z,t)$ and the higher modes is vanishingly small. This observation should be a subject of future rigorous studies.

IV. WEAKLY NONLINEAR DYNAMICS OF THE STRING

Here we consider solutions of the equation of motion (9) in the form $\psi = \mathcal{A}(\tilde{z}, \tilde{t})e^{i(k_0\tilde{z} - \omega_0\tilde{t})}$ with $\mathcal{A} \in \mathbb{C}$ in the so called adiabatic approximation, which implies $|\dot{\mathcal{A}}| \ll |\omega_0\mathcal{A}|$, $|\mathcal{A}'| \ll |k_0\mathcal{A}| \ll 1$. That is, we consider a modulated wave with a slowly varied (in space and time) envelope profile. It is known that for the case of nonlinear dispersion (11a), in the low-amplitude limit, the envelope wave is governed by the cubic nonlinear Schrödinger equation. The latter result can be obtained from the general Whitham approach in the low-amplitude limit [55,65,66], or within the formalism of nonlinear geometrical optics [67,68], or by means of the multiple-scales method [46,47]. Application of the method of multiple scales to (9) results in the following nonlinear Schrödinger equation (NLSE):

$$i[\dot{\mathcal{A}} + v_g(k_0)\mathcal{A}'] + \frac{\mu(k_0)}{2}\mathcal{A}'' + \nu(k_0)\mathcal{A}|\mathcal{A}|^2 = 0. \qquad (14)$$
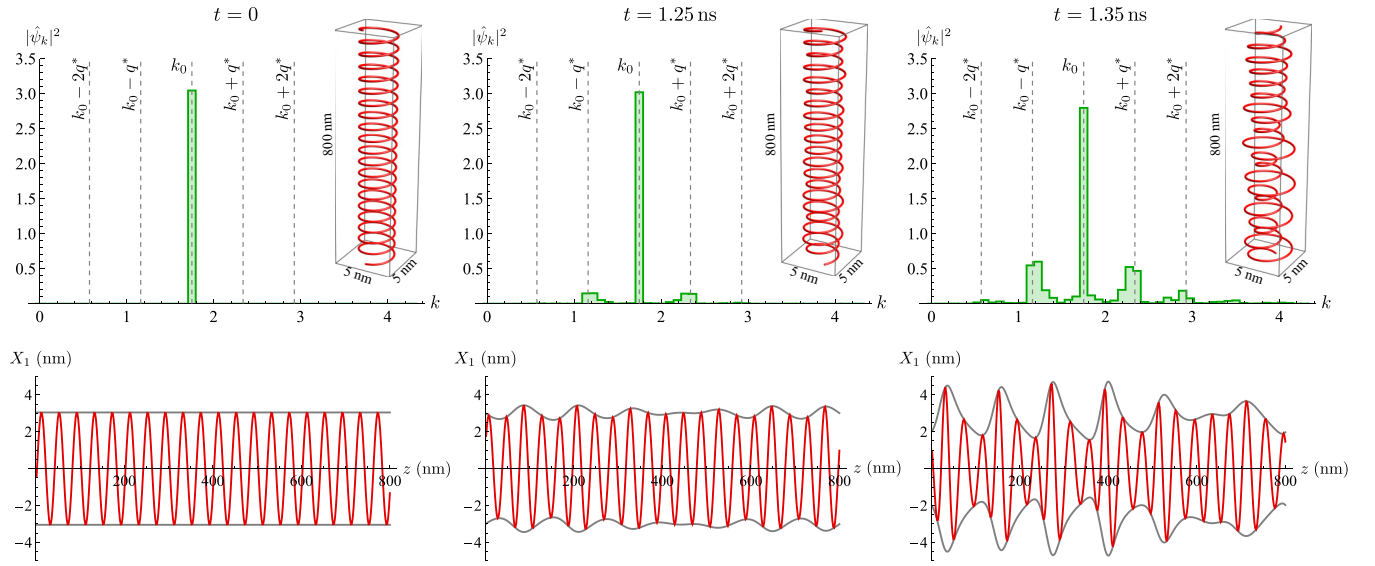
FIG. 6. Instability development of helical wave (10) obtained by means of micromagnetic simulations for FeGe (see Appendix E for details) in field $h = 2.16$ (0.8 T). The helix radius and wave vector are $\mathcal{R}_0 = 0.27$ (3 nm) and $k = k_0 = 1.75$ ($2\pi/40$ mnn^{-1}), respectively. For the considered parameters, $q^* \approx \mathcal{R}_0 k_0^2 \sqrt{b_1/a_1} \approx 0.59$. The dependencies $X_1(z)$ shown in the bottom (red line) are extracted from the simulation data with the use of Eq. (1). The envelope $R(z) = \sqrt{X_1^2 + X_2^2}$ is shown by the gray line.

Here the group velocity $v_g(k) = \partial_k \omega_0$ as well as coefficients $\mu(k) = \partial_k^2 \omega_0$ and $\nu(k) = k^2 \omega_1(k)$ are completely determined by the nonlinear dispersion (10). For details, see Appendix G. In the reference frame $\tilde{z}' = \tilde{z} - v_g(k_0)\tilde{t}$ which moves with the group velocity, the equation for amplitude $\mathcal{A}$ has the form of a classical NLSE,

$$i\dot{\mathcal{A}} + \frac{\mu(k_0)}{2}\mathcal{A}'' + \nu(k_0)\mathcal{A}|\mathcal{A}|^2 = 0. \tag{15}$$

Based on (11b) and (11c), and on the numerically obtained dependencies $a_n(h)$ and $b_n(h)$, we verified that $\mu(k_0) > 0$ and $\nu(k_0) > 0$ for $k_0 > k_c$, meaning that NLSE (15) is of a focusing type. The latter agrees with the Lighthill criterion (12).

Solutions of NLSE (15) are well studied and classified [69–71]. In the rest of this section, we use micromagnetic simulations in order to confirm the existence and verify the main properties of the string excitations in the form of the solutions predicted by NLSE (15).

A. Instability of the nonlinear helical wave

In the following, it is convenient to present the wave envelope in the form $\mathcal{A} = \mathcal{R}(\tilde{z}', \tilde{t})e^{i\phi(\tilde{z}', \tilde{t})}$, where $\mathcal{R}, \phi \in \mathbb{R}$. Equation (15) has a spatially uniform solution that corresponds to the helical wave considered in Sec. III. In this case, $\mathcal{R} = \mathcal{R}_0 = $ const and $\phi = \Omega\tilde{t}$, where $\Omega = \mathcal{R}_0^2 \nu(k_0) = \mathcal{R}_0^2 k_0^2 \omega_1(k_0)$ is a nonlinear shift of frequency of the helical wave. Introducing small deviations $\tilde{\mathcal{R}}$ and $\tilde{\phi}$ such that $\mathcal{R} = \mathcal{R}_0 + \tilde{\mathcal{R}}$ and $\phi = \Omega\tilde{t} + \tilde{\phi}$, we obtain from (15) the corresponding linearized equations for the deviations, whose solutions $\tilde{\mathcal{R}}, \tilde{\phi} \propto e^{i(q\tilde{z} - \tilde{\omega}\tilde{t})}$ are characterized by the dispersion relation

$$\tilde{\omega} = |q|\sqrt{q^2 \mu^2(k_0)/4 - \mu(k_0)\nu(k_0)\mathcal{R}_0^2}. \tag{16}$$

Thus, if the condition (12) holds, the helical wave is unstable for $|q| < q_0 = 2\mathcal{R}_0\sqrt{\nu(k_0)/\mu(k_0)} = 2\mathcal{R}_0|k_0|\sqrt{\omega_1(k_0)/\omega_0''(k_0)}$ and the maximum of the instability increment $\varkappa_{max} = \mathcal{R}_0^2 \nu(k_0)$ corresponds to $q^* = q_0/\sqrt{2}$.

We verified these predictions on the helical wave instability by means of micromagnetic simulations [72]. The initial magnetization state in the form of the helical wave was prepared as explained in Appendix F. Using (1), we extract the central string line $\mathbf{X}(z, t)$ from the simulation data of the magnetization dynamics. The time development of the modulational instability of the helical wave is shown in Fig. 6 in terms of $\mathbf{X}(z, t)$ and in terms of the corresponding $\psi(\tilde{z}, \tilde{t})$. Applying the Fourier transform $\hat{\psi}_k(\tilde{t}) = L_z^{-1} \int_0^{L_z} \psi(\tilde{z}, \tilde{t})e^{-ik\tilde{z}}d\tilde{z}$, we observe the development of the cascade of satellites at $k = k_0 \pm nq^*$, which is a signature of the modulation instability [55]. Note the good agreement of the satellites positions with the predictions (vertical dashed lines).

Note that the typical time of the instability development $\tau^* = 1/\varkappa_{max} \propto k_0^{-4}$ rapidly increases with the decrease of the wave vector. This feature was utilized for numerical determination of the coefficients a_n and b_n by means of the micromagnetic simulations. The values of k_0 used in these simulations were two to four times smaller than k_0 in Fig. 6; see Appendix F. Thus, the instability effects were negligible during the simulation time. Another way to avoid the helical wave instability is to simulate a short sample with the length $L_z = 2\pi/|k_0| < 2\pi/q_0$ and the periodic boundary conditions applied along z. In this case, the wave vectors $|q| < q_0$ of the unstable excitations do not exist in the system.

B. Cnoidal waves and solitons

As a generalization of the helical wave solution $\mathcal{A} = \mathcal{R}_0 e^{i\Omega\tilde{t}}$ with constant radius, NLSE (15) has a class of traveling-wave solutions with coordinate-dependent and static
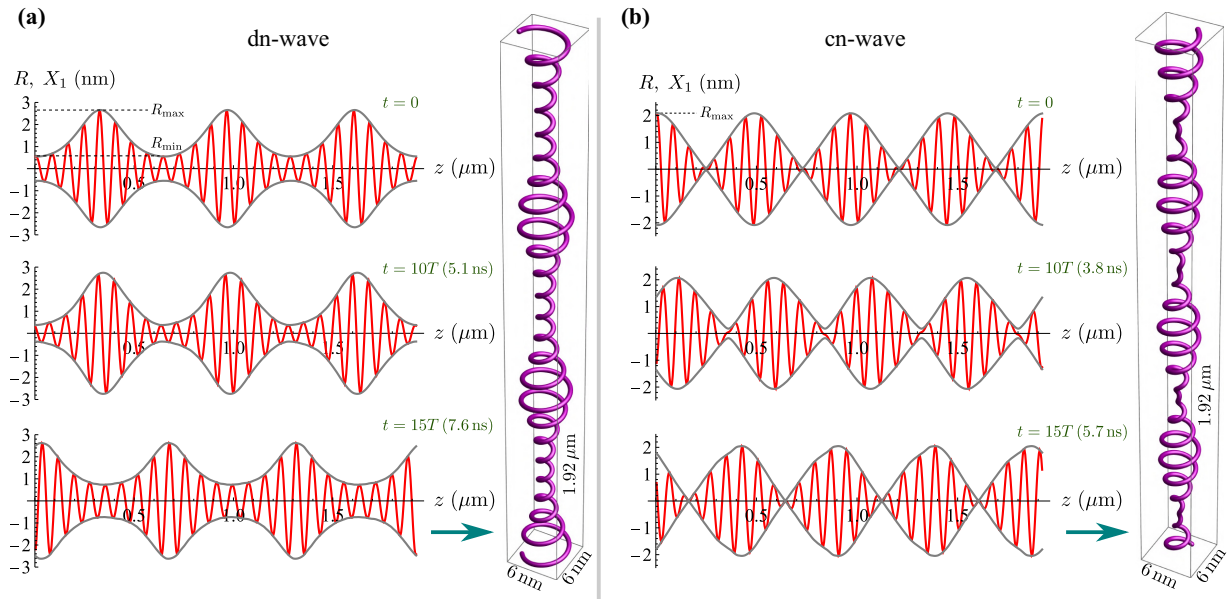
FIG. 7. Nonlinear waves of a skyrmion string in FeGe obtained by means of micromagnetic simulations (see Appendix E for details) for a magnetic field $\mu_0 H_{ext} = 0.8$ T. Red and gray lines in the plots have the same meaning as in Fig. 6. The upper plots ($t = 0$) in insets (a) and (b) show the initial perturbation of the skyrmion string. The perturbations are close to solutions (17) and (19), respectively. The lower plots demonstrate the snapshots taken at time moments $t = 10T$ and $15T$, with $T = L/v_g$ being the time it takes for a wave to cover a distance equal to its period L. The wavelength of the carrying wave is 80 nm ($k_0 = 0.875$). For both panels, the vertical insets show the 3D string shape at $t = 15T$. Note that the horizontal sizes are magnified 30 times. The dynamics of the dn- and cn-waves is demonstrated in the Supplemental movies 3 and 4, respectively [57].

(in the moving reference frame) profiles $\mathcal{A} = \mathcal{R}(\tilde{z}')e^{i\Omega\tilde{t}}$. Here the frequency $\Omega = \nu\mathcal{R}_0^2$ is the same as for the helical wave. The first integral of the corresponding equation for $\mathcal{R}(\tilde{z}')$ is $\mathcal{R}'^2 + W(\mathcal{R}) = \mathcal{E}_0$, where $W(\mathcal{R}) = \frac{\nu}{\mu}\mathcal{R}^2(\mathcal{R}^2 - 2\mathcal{R}_0^2)$. For NLSE (15) of a focusing type, constant $\mathcal{E}_0 > -\frac{\nu}{\mu}\mathcal{R}_0^4$ can be interpreted as the energy of an oscillator with potential well $W(\mathcal{R})$. Solutions for $\mathcal{R}(\tilde{z}')$ depend on two parameters $\mathcal{R}_0$ and $\mathcal{E}_0$, and they are divided into two classes depending on the sign of $\mathcal{E}_0$. The "negative energy" solutions have the profile

$$\mathcal{R}_{DN} = \mathcal{R}_{max}dn(\tilde{z}'/\Delta_{DN}, s_{DN}), \qquad (17)$$

where $dn(x, s)$ is a Jacobian elliptic function [73] with modulus $s_{DN} = \sqrt{1 - \mathcal{R}_{min}^2/\mathcal{R}_{max}^2}$, and $\Delta_{DN} = \mathcal{R}_{max}^{-1}\sqrt{\mu/\nu}$. Here, as an alternative to parameters $\mathcal{R}_0$ and $\mathcal{E}_0$, we use parameters $\mathcal{R}_{max}$ and $\mathcal{R}_{min}$, such that $\mathcal{R}_0^2 = (\mathcal{R}_{max}^2 + \mathcal{R}_{min}^2)/2$ and $\mathcal{E}_0 = -\frac{\nu}{\mu}\mathcal{R}_{max}^2\mathcal{R}_{min}^2$. Parameters $\mathcal{R}_{max}$ and $\mathcal{R}_{min}$ denote maximal and minimal amplitudes of the dn-wave; see Fig. 7(a). The wave period is $L_{DN} = 2\Delta_{DN}K(s_{DN})$, with $K(x)$ being the complete elliptic integral of the first kind. In the limit case $\mathcal{R}_{min} \rightarrow \mathcal{R}_{max}$, the cnoidal wave (17) transforms to the helical wave with an excitation of vanishing amplitude $\tilde{\mathcal{R}} = (\mathcal{R}_{max} - \mathcal{R}_{min})/2$ and wave vector $q = q_0$ corresponding to the edge of the helical wave instability. For the case $\mathcal{R}_{min} \ll \mathcal{R}_{max}$, the solution (17) has the form of a train of solitary waves separated by the distance $L_{DN} \approx 2\Delta_{DN}\ln(2\mathcal{R}_{max}/\mathcal{R}_{min})$. In the limit case $\mathcal{R}_{min} = 0$, the cnoidal wave (17) transforms to a soliton,

$$\mathcal{R}_{sol} = \frac{\mathcal{R}_{max}}{\cosh(\tilde{z}'/\Delta_{DN})}, \qquad (18)$$

with energy $\mathcal{E}_0 = 0$. So, soliton (18) is the separatrix solution between two classes of nonlinear waves with $\mathcal{E}_0 < 0$ and $\mathcal{E}_0 > 0$. In the latter case, the envelope profile is

$$\mathcal{R}_{CN} = \mathcal{R}_{max}cn(\tilde{z}'/\Delta_{CN}, s_{CN}), \qquad (19)$$

where $\Delta_{CN} = (\mathcal{R}_{max}^2 + \mathcal{R}_{min}^2)^{-1/2}\sqrt{\mu/\nu}$ and $s_{CN} = 1/\sqrt{1 + \mathcal{R}_{min}^2/\mathcal{R}_{max}^2}$. Here the parameters $\mathcal{R}_{max}$ and $\mathcal{R}_{min}$ are chosen such that $\mathcal{R}_0^2 = (\mathcal{R}_{max}^2 - \mathcal{R}_{min}^2)/2$ and $\mathcal{E}_0 = \frac{\nu}{\mu}\mathcal{R}_{max}^2\mathcal{R}_{min}^2$. In contrast to dn-waves (17), the profile of cn-wave (19) has nodes where $\mathcal{R}_{CN} = 0$. The distance between nodes is $L_{CN}/2 = 2\Delta_{CN}K(s_{CN})$. In the limit case $\mathcal{R}_{min} = 0$, cn-wave (19) is transformed into soliton (18). In the literature, the nonlinear waves (17) and (19) described by the elliptical functions are known as "cnoidal waves." They are common for different physical media, with the widely known examples being shallow water [46,66] and atmosphere [74].

Solutions (17), (19), and (18) represent a partial case of traveling waves moving exactly with the group velocity $v_g(k_0)$. The generalization for the case of arbitrary velocity is realized by means of the replacement $\tilde{z}' \rightarrow \tilde{z}' - V\tilde{t}$. In this case, $\phi = \Omega\tilde{t} + \frac{V}{\mu}(\tilde{z}' - \frac{V}{2}\tilde{t})$. Note that V is the envelope velocity in the moving reference frame $\tilde{z}' = \tilde{z} - v_g(k_0)\tilde{t}$. Three parameters $\mathcal{R}_{max}$, $\mathcal{R}_{min}$, and V are stabilized by three integrals of motion, the number of excitations $N = \int_0^{L_z} \mathcal{R}^2 d\tilde{z}'$, momentum $P = -\frac{V}{\mu}N$, and energy $E = \frac{V^2}{2\mu}N + \frac{1}{2}\int_0^{L_z}(\mu\mathcal{R}'^2 - \nu\mathcal{R}^4)d\tilde{z}'$.

To verify the predictions of the NLSE (15) considered above, we performed a number of micromagnetic simulations [75]. The initial state was created programmatically
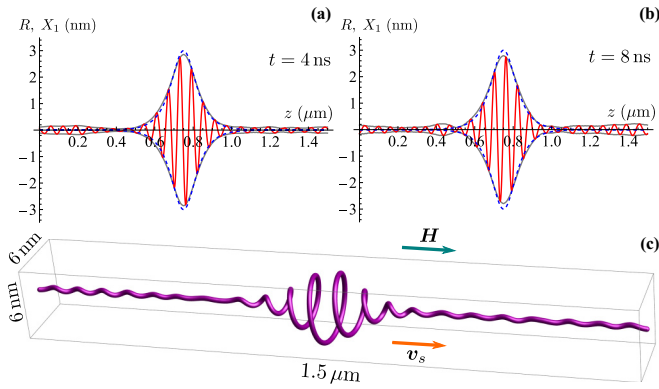
FIG. 8. Soliton solution (18) obtained by means of micromagnetic simulations of a skyrmion string in FeGe (see Appendix E for details) in a magnetic field $\mu_0 H = 0.8$ T. The dashed blue line shows the initial soliton profile; the other notations are the same as in Fig. 7. Insets (a) and (b) shows the snapshots taken in different moments of time starting from the beginning of the simulations. Panel (c) is the 3D version of the inset (a). The wave vector of the carrying wave $k_0 = 1.17$ (wavelength 60 nm) corresponds to the group velocity $v_g = 2.2$ (1.64×10^3 m/s). The latter is close to the soliton velocity $v_s = 2.1$ (1.52×10^3 m/s) found in the simulations. The soliton dynamics is shown in movie 5 [57].

in the form of a skyrmion string, whose shape corresponds approximately to the theoretically predicted solution for a dn- or cn-wave with the profiles determined by (17) or (19), respectively. Then for a short time (≈ 10 ps), the micromagnetic dynamics was relaxed, i.e., run with high Gilbert damping ($\alpha_G = 0.5$). In the next step, the damping was switched off and the micromagnetic dynamics was simulated for a long time (10 ns). The technical details of the simulations can be found in Appendix E. We observe the propagation of the created nonlinear wave with an almost unchanged envelope profile; see Fig. 7. The latter says that the initially created wave is a solution of the equations of string dynamics. The slight profile deformation during dynamics takes place because of deviation of the initial states from the exact solutions. This deviation is approximately 10%, and it appears unavoidably due to the relaxation procedure applied on the second step. The dynamics of the cnoidal waves extracted from the simulations are demonstrated in the Supplemental movies 3 and 4 [57].

The propagation of solitons along the skyrmion string was considered in detail in our previous work [45]; see also the Supplemental movies in Ref. [45]. However, for the sake of completeness, we present here an example of the soliton dynamics obtained by means of micromagnetic simulations; see Fig. 8. The initial state was close to solution (18) with $\mathcal{R}_{\max} = 0.27$ (3 nm) and $\Delta_{DN} = 5.17$ (57.6 nm). These parameters are consistent with the wave vector $k_0 = 1.17$ ($\frac{2\pi}{60\,\text{nm}}$) of the carrying wave. Note that the soliton keeps its shape close to the initial profile (blue dashed line). Due to the imperfectness of the initial state and the discreteness effects, the low-amplitude magnons are generated on background. The corresponding energy loss leads to an insignificant reduction of the soliton amplitude; see panels (a) and (b) in Fig. 8. The complete time evolution of the soliton propagation is shown in Supplemental movie 5 [57].

C. A breather solution

The solutions of the NLSE (15) considered above have the form of traveling waves, i.e., there is a frame of reference in which the envelope wave $|\mathcal{A}|$ is static. Here we consider breathers—the family of solutions beyond the class of traveling waves. There are several kinds of breathers of the NLSE: localized in space and periodic in time Ma breathers [76], a localized in time and periodic in space Akhmediev breather [70], and a Peregrine solution that is localized in both space and time [77]. In the following, we focus on the Ma breather, which is a spatially localized periodically pulsating perturbation of a helical wave in the form [76] $\mathcal{A}_{MA} = \mathcal{R}_0 \varrho(\tilde{z}', \tilde{t}) e^{i\Omega \tilde{t}}$, where $\Omega = \nu(k_0)\mathcal{R}_0^2$ is the same as for the helical wave, and

$$\varrho(\tilde{z}', \tilde{t}) = \frac{\cos(\Omega_{MA}\tilde{t} - 2i\varphi) + \cosh(\tilde{z}'/\Delta_{MA})\cosh\varphi}{\cos(\Omega_{MA}\tilde{t}) + \cosh(\tilde{z}'/\Delta_{MA})\cosh\varphi}. \quad (20)$$

In addition to the characteristics of the carrying wave $\mathcal{R}_0$ and k_0, the breather solution is controlled also by the real-valued parameter φ. These parameters determine the pulsation frequency $\Omega_{MA} = \Omega \sinh(2\varphi)$ and the breather width $\Delta_{MA} = \Delta_{DN}/(2\sinh\varphi)$. The breather amplitude $\mathcal{A}_{MA}^0 = |\mathcal{A}_{MA}(\tilde{z}' = 0)|$ varies in the range $\mathcal{R}_0(2\cosh\varphi - 1) \leqslant \mathcal{A}_{MA}^0 \leqslant \mathcal{R}_0(2\cosh\varphi + 1)$ during the pulsations. The considered breather moves with the group velocity. The generalization for the case of arbitrary velocity V is the same as for the traveling-wave solutions.

Using micromagnetic simulations, we found the Ma breather for a skyrmion string in FeGe; see Fig. 9. A very good agreement between the simulated and theoretical breather profiles [Figs. 9(a)–9(d)] as well as the observed periodic breathing behavior prove that the Ma breather is indeed a solution of the skyrmion string dynamics. Nevertheless, one has to note that in simulations the breather develops instability after the first three breathing periods. This instability has several sources. In contrast to solitons, the breather is the excitation of the helical wave of a *finite* amplitude. As was shown above, such waves demonstrate modulational instability. Also, for technical reasons related to the limited computational resources, we were able to simulate a breather for the relatively large wave vector of the carrying wave, $k_0 = 1.75$. Since $k_0 \mathcal{A}_{MA}^0 \approx 0.71$, we are at the edge of applicability of the developed theory, which implies $|k_0 \mathcal{A}| \ll 1$. Due to the large value of k_0, one can only approximately estimate linear $\omega_0(k_0)$ and nonlinear $\omega_1(k_0)$ parts of the dispersion if only the few first terms in (11) are taken into account. This is the reason why the theoretically expected period of the breathing $2\pi/\Omega_{MA} \approx 0.49$ ns differs from the period $T_{MA} \approx 0.76$ ns obtained in the simulations.

V. COLLECTIVE DYNAMICS OF GENERALIZED STRINGS

Previously we considered the case when the collective variables $X_i(z, t)$ have a sense of the string displacement in the xy-plane. Let us now consider a generalized ansatz

$$\boldsymbol{m}(\boldsymbol{r}, t) = \boldsymbol{m}_0(x, y, X_i(z, t), X_i'(z, t)), \quad (21)$$

where $\boldsymbol{m}_0$ is a known function, and the string collective variables X_i can have an arbitrary sense. In this section, we use a prime and an overdot for the derivatives with re-
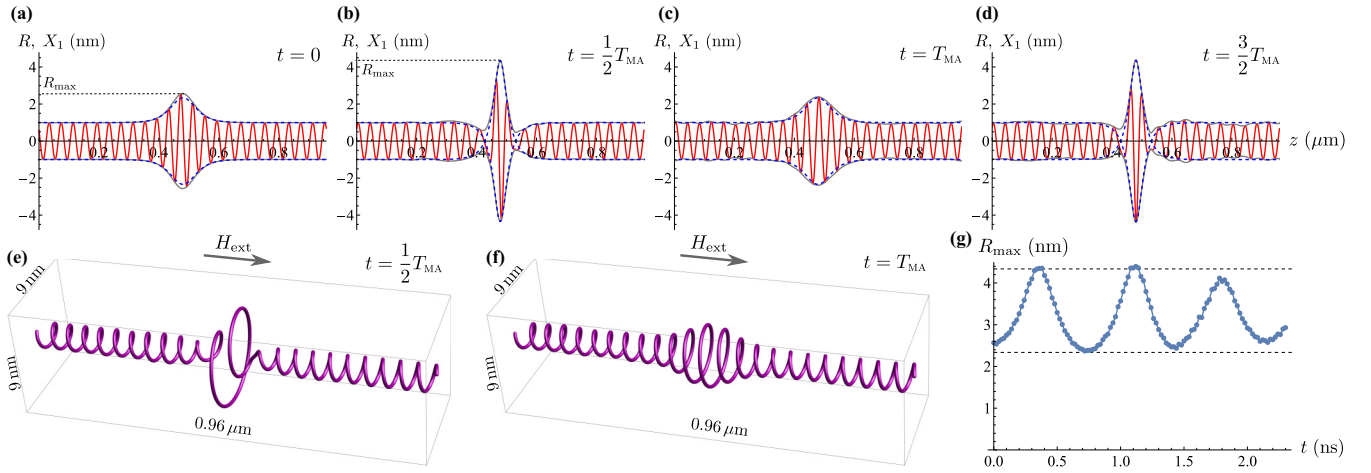
FIG. 9. (a)–(d) Micromagnetic simulations (see Appendix E for details) of the time evolution of Ma breather along the skyrmion string in FeGe for $\mu_0 H_{ext} = 0.8$ T. The carrying helical wave has amplitude $R_0 = 1$ nm ($\mathcal{R}_0 = 0.01$) and pitch 40 nm ($k_0 = 1.75$). We consider the case $\varphi = 1.1$. The dashed blue line shows the theoretically predicted profile $R = |\mathcal{A}_{MA}|/Q$ determined by (20) for given parameters, while the solid red and gray lines represent the simulation data; they have the same meaning as in Figs. 6 and 7. Insets (e) and (f) show the 3D structure of the breather for the time moments corresponding to the maximal and minimal amplitude. Note the $30\times$ magnification in the directions perpendicular to the magnetic field. Breathers move with the group velocity $v_g(k_0)$; however, in each snapshot the breather is shown in the center of the sample for better visual perception. Inset (g) shows the time evolution of the breather amplitude $R_{max} = \mathcal{A}_{MA}^0/Q$. Dashed horizontal lines indicates the theoretically predicted boundaries for the breather amplitude; see the discussion in the text. The period of the simulated breather is $T_{MA} = 0.76$ ns. The breather dynamics is shown in Supplemental movie 6 [57].

spect to z and t, respectively. The equation of motion for X_i can be formulated in the general form $\delta\mathfrak{S}/\delta X_i = \delta\mathfrak{F}/\delta\dot{X}_i$, where $\mathfrak{S} = \int dt \int dz\mathcal{L}$ is the action with the Lagrangian $\mathcal{L} = \frac{M_s}{\gamma_0} \iint [\mathfrak{A}(\boldsymbol{m}) \cdot \dot{\boldsymbol{m}}]dxdy - \mathcal{H}$, and $\mathfrak{F} = \int dz\mathcal{F}$ is the dissipation function with $\mathcal{F} = \frac{\alpha}{2}\frac{M_s}{\gamma_0} \iint \dot{\boldsymbol{m}}^2 dxdy$. Here the vector potential $\mathfrak{A}$ is such that $\boldsymbol{m} \cdot (\nabla_{\boldsymbol{m}} \times \mathfrak{A}) = 1$, and the system Hamiltonian is $H = \int dz\mathcal{H}$. For the model (21), the equations of motion have the following form

$$[G_{ij}^{(0)} + (G_{ji}^{(1)})']\dot{X}_j + [G_{ij}^{(1)} + G_{ji}^{(1)} - (G_{ij}^{(2)})']\dot{X}_j' - G_{ij}^{(2)}\dot{X}_j''$$
$$= \frac{\delta H}{\delta X_i} + \alpha\{[D_{ij}^{(0)} - (D_{ji}^{(1)})']\dot{X}_j$$
$$+ [D_{ij}^{(1)} - D_{ji}^{(1)} - (D_{ij}^{(2)})']\dot{X}_j' - D_{ij}^{(2)}\ddot{X}_j''\}; \qquad (22)$$

for details, see Appendix H. The gyroscopic $G_{ij}^{(n)}$ and dissipation $D_{ij}^{(n)}$ tensors are functionals of X_i and their derivatives, and they are listed in (H3) in Appendix H. Tensors $G_{ij}^{(0)} = -G_{ji}^{(0)}$ and $G_{ij}^{(2)} = -G_{ji}^{(2)}$ are asymmetrical by definition, while tensors $D_{ij}^{(0)} = D_{ji}^{(0)}$ and $D_{ij}^{(2)} = D_{ji}^{(2)}$ are symmetrical. Note that $(G_{ij}^{(n)})' \propto X_i', X_i''$ and $(D_{ij}^{(n)})' \propto X_i', X_i''$, so these terms in (22) result in the nonlinear corrections.

A. Radially symmetrical excitation of the skyrmion string

As an example of an application of the generalized equations (22), we consider the dynamics of the radially symmetrical deformation of the string. It can be described by the following ansatz:

$$\theta = \theta_0(\rho/s), \quad \phi = \chi + \frac{\pi}{2} + \varphi, \qquad (23)$$

where θ and ϕ are the spherical angles of the parametrization $\boldsymbol{m} = \sin\theta(\cos\phi\hat{\boldsymbol{x}} + \sin\phi\hat{\boldsymbol{y}}) + \cos\theta\hat{\boldsymbol{z}}$, and (ρ, χ) are polar coordinates within the xy-plane. Here, $\theta_0(\rho)$ is the profile of the unperturbed skyrmion, and $s(z, t) = X_1$ and $\varphi(z, t) = X_2$ are the collective string variables. According to (H3), we have $G_{ij}^{(0)} = 2\pi\epsilon_{ij}|\mathfrak{c}|sM_s/(\gamma_0 Q^2)$ and $G_{ij}^{(1)} = G_{ij}^{(2)} = 0$. Here $\mathfrak{c} = \int_0^\infty \tilde{\rho}^2 \sin\theta_0\theta_0'(\tilde{\rho})d\tilde{\rho} < 0$, where $\tilde{\rho} = Q\rho$.

In what follows, we neglect damping for simplicity. In terms of the dimensionless time $\tilde{t} = t\omega_{c2}$ and coordinate $\tilde{z} = zQ$, we write the equations of motion (22) in the form

$$2|\mathfrak{c}|s\partial_{\tilde{t}}\varphi = \frac{\delta\tilde{H}}{\delta s}, \quad -2|\mathfrak{c}|s\partial_{\tilde{t}}s = \frac{\delta\tilde{H}}{\delta\varphi}, \qquad (24)$$

where the dimensionless Hamiltonian is

$$\tilde{H} = \int_{-\infty}^\infty d\tilde{z}\{e_{ex} + \mathfrak{c}_1(\partial_{\tilde{z}}s)^2 + \mathfrak{c}_2 s^2[(\partial_{\tilde{z}}\varphi)^2 - 2\partial_{\tilde{z}}\varphi]$$
$$+ 2e_{dmi}s\cos\varphi + 2e_z hs^2\}. \qquad (25)$$

To obtain the effective Hamiltonian (25) for the collective string variables s and φ, we substitute ansatz (23) into the main Hamiltonian (6) and perform the integration over the xy-plane. Finally, we obtain $H = 2\pi AQ^{-1}\tilde{H}$. The constants $e_{ex} = \mathcal{H}_{ex}^{(0)}/4$, $e_{dmi} = \mathcal{H}_{DMI}^{(0)}/4$, and $e_z = \mathcal{H}_z^{(0)}/4$ represent (up to a constant multiplier) the exchange, DMI, and Zeeman energies of the unperturbed skyrmion string, respectively; see Appendix D for the definitions of $\mathcal{H}_\bullet^{(0)}$. The other constants are $\mathfrak{c}_1 = \int_0^\infty \tilde{\rho}^3 \theta_0'(\tilde{\rho})^2 d\tilde{\rho}$ and $\mathfrak{c}_2 = \int_0^\infty \tilde{\rho} \sin^2\theta_0 d\tilde{\rho}$.

The explicit form of the equations of motion (24) is

$$|\mathfrak{c}|s\partial_{\tilde{t}}s = \mathfrak{c}_2 s^2\partial_{\tilde{z}}^2\varphi - 2\mathfrak{c}_2 s\partial_{\tilde{z}}s(1 - \partial_{\tilde{z}}\varphi) - |e_{dmi}|s\sin\varphi,$$
$$|\mathfrak{c}|s\partial_{\tilde{t}}\varphi = -\mathfrak{c}_1\partial_{\tilde{z}}^2 s + \mathfrak{c}_2 s[(\partial_{\tilde{z}}\varphi)^2 - 2\partial_{\tilde{z}}\varphi]$$
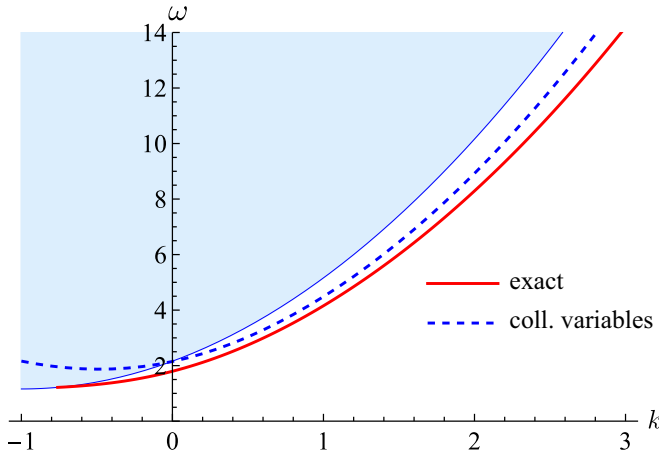$$+ |e_{dmi}|(s - \cos\varphi). \qquad (26)$$

FIG. 10. The dispersion relation of the breathing mode for $h = 2.16$ ($\mu_0 H_{\text{ext}} = 0.8$ T) (solid line) is compared to the collective variables approximation (27) (dashed line) with the following values of the constants: $\mathfrak{c} \approx -0.684$, $\mathfrak{c}_1 \approx 1.299$, $\mathfrak{c}_2 \approx 0.397$, $e_{\text{dmi}} \approx -1.477$. The "exact" solution is the same as in Fig. 3(a).

Writing (26), we exclude e_z by means of the virial relation $2he_z + e_{\text{dmi}} = 0$ and we use that $e_{\text{dmi}} < 0$. The solution $s = 1$ and $\varphi = 0$ corresponds to the ground state if $h > 1$.

Next, we introduce small deviations $s = 1 + \tilde{s}$ and $\varphi = \tilde{\varphi}$ on the top of the ground state. The linearization of (26) with respect to the deviations results in the planar wave solutions $\tilde{s}, \tilde{\varphi} \propto e^{i(k\tilde{z} - \omega\tilde{t})}$ with the dispersion relation

$$|\mathfrak{c}|\omega = 2\mathfrak{c}_2 k + \sqrt{(\mathfrak{c}_1 k^2 + |e_{\text{dmi}}|)(\mathfrak{c}_2 k^2 + |e_{\text{dmi}}|)}$$

$$\approx |e_{\text{dmi}}| + 2\mathfrak{c}_2 k + \frac{\mathfrak{c}_1 + \mathfrak{c}_2}{2}k^2. \qquad (27)$$

Note that $\mathfrak{c}_1 + \mathfrak{c}_2$ is the second moment of the exchange energy density of the unperturbed string. The comparison of the approximated dispersion (27) with the exact one is shown in Fig. 10.

Equations of motion (24) are Euler-Lagrange equations of the Lagrange function

$$\mathfrak{L} = |\mathfrak{c}| \int_{-\infty}^{\infty} s^2 \partial_{\tilde{t}} \varphi \, d\tilde{z} - \tilde{H}. \qquad (28)$$

The invariance of the Lagrange function with respect to translations along $\tilde{t}$ and $\tilde{z}$ results in two integrals of motion, namely energy $E = \tilde{H}$ and momentum $P = -|\mathfrak{c}| \int_{-\infty}^{\infty} s^2 \partial_{\tilde{z}} \varphi \, d\tilde{z}$. From the latter expression, we derive $\delta P = 2|\mathfrak{c}| \int_{-\infty}^{\infty} s[\partial_{\tilde{z}} s\delta\varphi - \partial_{\tilde{z}}\varphi\delta s]d\tilde{z}$. On the other hand, we can write $\delta E = \int_{-\infty}^{\infty} [\frac{\delta\tilde{H}}{\delta\varphi}\delta\varphi + \frac{\delta\tilde{H}}{\delta s}\delta s]d\tilde{z}$, and with the help of (24) we obtain $\delta E = V\delta P$ for the traveling-wave solutions $s = s(\tilde{z} - V\tilde{t})$ and $\varphi = \varphi(\tilde{z} - V\tilde{t})$. Thus, we obtain a Hamiltonian equation $V = \partial E/\partial P$. Note that the second Hamiltonian equation is $\partial_{\tilde{t}} P = 0$ due to the momentum conservation.

For the traveling-wave solutions, functions $s(\tilde{z}')$ and $\varphi(\tilde{z}')$ are determined by the equations

$$|\mathfrak{c}|Vss' = -\mathfrak{c}_2 s^2 \varphi'' + 2\mathfrak{c}_2 ss'(1 - \varphi') + |e_{\text{dmi}}|s\sin\varphi,$$
$$|\mathfrak{c}|Vs\varphi' = \mathfrak{c}_1 s'' - \mathfrak{c}_2 s[\varphi'^2 - 2\varphi'] - |e_{\text{dmi}}|(s - \cos\varphi), \qquad (29)$$
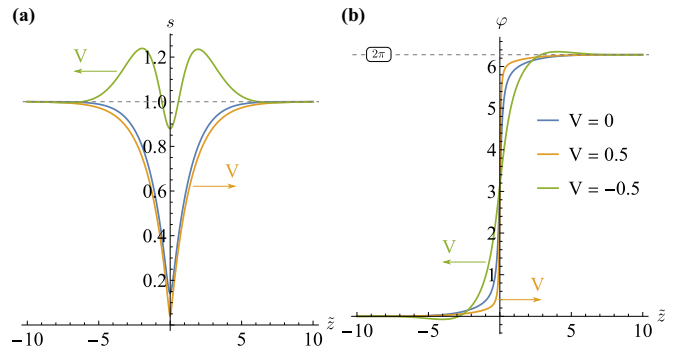

FIG. 11. Topological solutions of Eqs. (29) in form of a 2π-domain wall are obtained for different V. We consider the case with $h = 1.05$ corresponding to $\mathfrak{c} \approx -3.34$, $\mathfrak{c}_1 \approx 7.4$, $\mathfrak{c}_2 \approx 1.67$, and $e_{\text{dmi}} \approx -3.51$.

where a prime denotes the derivative with respect to $\tilde{z}' = \tilde{z} - V\tilde{t}$. Note that it is technically easier to find the numerical solutions $s(\tilde{z}')$ and $\varphi(\tilde{z}')$ as minimizers of the effective energy $E_{\text{eff}} = E - VP$.

Equations (29) have solutions in the form of a 2π-domain wall (DW), which encircles the skyrmion tube; see Fig. 11. In the center of the DW, $\phi = \pi$, see Fig. 11(b), meaning that the skyrmion helicity there is opposite to the equilibrium one. The latter results in a significant increase of the DMI energy. As a result, the skyrmion tube shrinks at the DW position in order to reduce the DMI energy; see Fig. 11(a). On the other hand, the skyrmion tube shrinking leads to an increase of the magnetization gradients, and therefore to an increase of the exchange energy. The competition between exchange and DMI results in a small but nonvanishing radius of the skyrmion tube in the domain-wall center. Remarkably, the DW motion against the applied magnetic field ($V < 0$) can significantly increase the skyrmion tube radius in the DW position; see the case $V = -0.5$ in Fig. 11(a). The latter effect is promising for avoiding the skyrmion string breaking in possible experimental realization of the considered DW.

VI. CONCLUSIONS

We have shown that the low-energy dynamics of a translational mode propagating along a skyrmion string is captured by the focusing-type nonlinear Schrödinger equation (NLSE). As a result, a number of solutions of the NLSE are found and confirmed by means of micromagnetic simulations, namely cnoidal waves, solitons, and breathers. Finally, we proposed a generalized approach that enables one to describe the nonlinear dynamics of the modes of different symmetries, i.e., radially symmetric, elliptical, etc.

The approach proposed herein has a wide spectrum of future perspectives: (i) it can be applied for antiskyrmion strings as well as for meron strings, (ii) it can be adapted for antiferromagnetic skyrmion or meron strings, (iii) it can be used to analyze the weakly nonlinear dynamics of higher modes of the strings. Although the surface effects were not considered in this study, the possible interaction of string solitons with the magnet boundary, e.g., the effect of reflection, can be a subject of a further study.

APPENDIX A: POISSON BRACKETS FOR THE STRING COLLECTIVE VARIABLES

As a direct consequence of (3), one can show that the Poisson brackets of any two functionals $F[\boldsymbol{m}]$, $G[\boldsymbol{m}]$ are [78]

$$\{F, G\} = -\frac{\gamma_0}{M_s} \int \boldsymbol{m} \cdot \left[\frac{\delta F}{\delta \boldsymbol{m}} \times \frac{\delta G}{\delta \boldsymbol{m}} \right] d\boldsymbol{r}. \tag{A1}$$

The string coordinates (1) can be considered as functionals of magnetization:

$$X_i(z) = \frac{1}{N_{\text{top}}} \int x_i' g_z(\boldsymbol{r}') \delta(z - z') d\boldsymbol{r}'. \tag{A2}$$

Straightforward calculation of the functional derivative results in

$$\frac{\delta X_i(z)}{\delta \boldsymbol{m}(z')} = \frac{1}{4\pi N_{\text{top}}} \{3 x_i [\partial_x \boldsymbol{m} \times \partial_y \boldsymbol{m}]$$
$$+ \epsilon_{ij} [\boldsymbol{m} \times \partial_{x_j} \boldsymbol{m}] \} \delta(z - z'). \tag{A3}$$

The usage of (A3) in (A1) results in (4).

APPENDIX B: DEFINITION AND PROPERTIES OF THE CURVILINEAR COORDINATES

The aim of this Appendix is to introduce a curvilinear frame of reference that follows the form of a string. Such a reference frame is convenient for the formulation of the skyrmion string ansatz and for calculation of the string energy.

Let us consider a 3D curve $\boldsymbol{\gamma} : \mathbb{R} \to \mathbb{R}^3$ parametrized by means of the scalar parameter $-\infty < \zeta < \infty$ in the following manner: $\boldsymbol{\gamma}(\zeta) = \boldsymbol{X}(\zeta) + \zeta \hat{\boldsymbol{z}}$, where $\boldsymbol{X}(\zeta) = X_1(\zeta)\hat{\boldsymbol{x}} + X_2(\zeta)\hat{\boldsymbol{y}}$. The unit vector tangential to the string is

$$\boldsymbol{e}_{\text{T}}(\zeta) = \frac{\boldsymbol{X}' + \hat{\boldsymbol{z}}}{\sqrt{1 + |\boldsymbol{X}'|^2}}. \tag{B1}$$

Here and below, a prime denotes derivative with respect to ζ. Within the plane perpendicular to $\boldsymbol{e}_{\text{T}}$, we introduce two
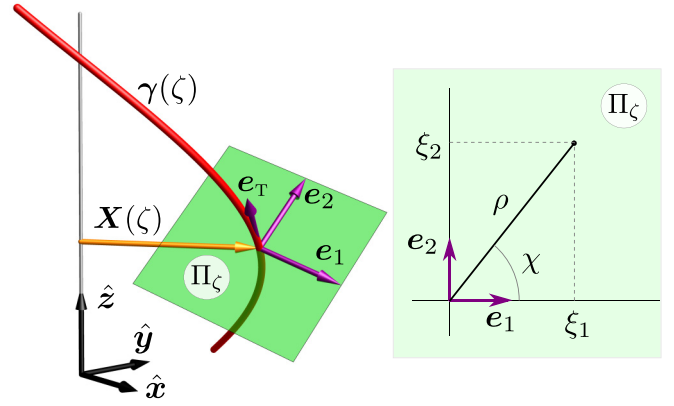

FIG. 12. Geometrical meaning of the notations used in Appendixes B and C as well as in the main text.

orthogonal unit vectors $\boldsymbol{e}_1$ and $\boldsymbol{e}_2$ as follows:

$$\boldsymbol{e}_1(\zeta) = \frac{\hat{\boldsymbol{x}} - \boldsymbol{e}_{\text{T}}(\boldsymbol{e}_{\text{T}} \cdot \hat{\boldsymbol{x}})}{\sqrt{1 - (\boldsymbol{e}_{\text{T}} \cdot \hat{\boldsymbol{x}})^2}}, \quad \boldsymbol{e}_2(\zeta) = \boldsymbol{e}_{\text{T}} \times \boldsymbol{e}_1. \tag{B2}$$

That is, vector $\boldsymbol{e}_1$ is the normalized projection of the Cartesian basis vector $\hat{\boldsymbol{x}}$ on the plane perpendicular to $\boldsymbol{e}_{\text{T}}$. The Cartesian and local bases are illustrated in Fig. 12. We parametrize the space domain, which includes curve $\boldsymbol{\gamma}$ and its vicinity, as $\boldsymbol{r}(\xi_1, \xi_2, \zeta) = \boldsymbol{\gamma}(\zeta) + \xi_1 \boldsymbol{e}_1(\zeta) + \xi_2 \boldsymbol{e}_2(\zeta)$, where ξ_1, ξ_2, ζ are local coordinates of the frame of reference defined on the string. In other words, (ξ_1, ξ_2) are coordinates within the plane Π_ζ perpendicular to the string that crosses the string in point $\boldsymbol{r} = \boldsymbol{\gamma}(\zeta)$.

The explicit form of the relation between coordinates $\{x, y, z, t\}$ of the laboratory frame of reference and coordinates $\{\xi_1, \xi_2, \zeta, \tau\}$ of the string frame of reference is

$$
\begin{aligned}
x &= X_1(\zeta, \tau) + (\boldsymbol{e}_1 \cdot \hat{\boldsymbol{x}})\xi_1 + (\boldsymbol{e}_2 \cdot \hat{\boldsymbol{x}})\xi_2, \\
y &= X_2(\zeta, \tau) + (\boldsymbol{e}_1 \cdot \hat{\boldsymbol{y}})\xi_1 + (\boldsymbol{e}_2 \cdot \hat{\boldsymbol{y}})\xi_2, \\
z &= \zeta + (\boldsymbol{e}_1 \cdot \hat{\boldsymbol{z}})\xi_1 + (\boldsymbol{e}_2 \cdot \hat{\boldsymbol{z}})\xi_2, \\
t &= \tau,
\end{aligned}
\tag{B3}
$$

where $\boldsymbol{e}_i = \boldsymbol{e}_i(\zeta, \tau)$. So, on the curve $\boldsymbol{\gamma}$ one has $(\xi_1, \xi_2) = (0, 0)$ and $\zeta = z$.

The differentials of the coordinates are related via Jacobian J:

$$
\begin{bmatrix} dx \\ dy \\ dz \\ dt \end{bmatrix} = J \begin{bmatrix} d\xi_1 \\ d\xi_2 \\ d\zeta \\ d\tau \end{bmatrix}, \quad J = \begin{bmatrix} (\boldsymbol{e}_1 \cdot \hat{\boldsymbol{x}}) & (\boldsymbol{e}_2 \cdot \hat{\boldsymbol{x}}) & X_1' + (\boldsymbol{e}_1' \cdot \hat{\boldsymbol{x}})\xi_1 + (\boldsymbol{e}_2' \cdot \hat{\boldsymbol{x}})\xi_2 & \partial_\tau X_1 + (\partial_\tau \boldsymbol{e}_1 \cdot \hat{\boldsymbol{x}})\xi_1 + (\partial_\tau \boldsymbol{e}_2 \cdot \hat{\boldsymbol{x}})\xi_2 \\ (\boldsymbol{e}_1 \cdot \hat{\boldsymbol{y}}) & (\boldsymbol{e}_2 \cdot \hat{\boldsymbol{y}}) & X_2' + (\boldsymbol{e}_1' \cdot \hat{\boldsymbol{y}})\xi_1 + (\boldsymbol{e}_2' \cdot \hat{\boldsymbol{y}})\xi_2 & \partial_\tau X_2 + (\partial_\tau \boldsymbol{e}_1 \cdot \hat{\boldsymbol{y}})\xi_1 + (\partial_\tau \boldsymbol{e}_2 \cdot \hat{\boldsymbol{y}})\xi_2 \\ (\boldsymbol{e}_1 \cdot \hat{\boldsymbol{z}}) & (\boldsymbol{e}_2 \cdot \hat{\boldsymbol{z}}) & 1 + (\boldsymbol{e}_1' \cdot \hat{\boldsymbol{z}})\xi_1 + (\boldsymbol{e}_2' \cdot \hat{\boldsymbol{z}})\xi_2 & (\partial_\tau \boldsymbol{e}_1 \cdot \hat{\boldsymbol{z}})\xi_1 + (\partial_\tau \boldsymbol{e}_2 \cdot \hat{\boldsymbol{y}})\xi_2 \\ 0 & 0 & 0 & 1 \end{bmatrix}. \tag{B4}
$$

Determinant $|J|$ determines the volume element in the curvilinear frame of reference, namely $dx \, dy \, dz \, dt = |J| d\xi_1 \, d\xi_2 \, d\zeta \, d\tau$. For small derivatives of X_i we can write $|J| = 1 - (\xi_1 X_1'' + \xi_2 X_2'') + \frac{1}{2}|X'|^2 + \cdots$. Note that due to the structure of Jacobian (B4), one has $dt = d\tau$ and therefore $dx \, dy \, dz = |J| d\xi_1 \, d\xi_2 \, d\zeta$.

Elements of the inverted Jacobian determine derivatives with respect to the Cartesian coordinates:

$$
J^{-1} = \begin{bmatrix}
\partial_x \xi_1 & \partial_y \xi_1 & \partial_z \xi_1 & \partial_t \xi_1 \\
\partial_x \xi_2 & \partial_y \xi_2 & \partial_z \xi_2 & \partial_t \xi_2 \\
\partial_x \zeta & \partial_y \zeta & \partial_z \zeta & \partial_t \zeta \\
\partial_x \tau & \partial_y \tau & \partial_z \tau & \partial_t \tau
\end{bmatrix}
$$

$$
= \begin{bmatrix}
1 & 0 & -X_1' & -\partial_\tau X_1 \\
0 & 1 & -X_2' & -\partial_\tau X_2 \\
X_1' & X_2' & 1 + \xi_1 X_1'' + \xi_2 X_2'' & \xi_1 \partial_\tau X_1' + \xi_2 \partial_\tau X_2' \\
0 & 0 & 0 & 1
\end{bmatrix}
$$

$$
+ o(X). \tag{B5}
$$

Thus, we find that the spatial derivatives are related as

$$
\partial_x = \partial_{\xi_1} + X_1' \partial_\zeta + o(X),
$$

$$
\partial_y = \partial_{\xi_2} + X_2' \partial_\zeta + o(X),
$$

$$
\partial_z = -X_1' \partial_{\xi_1} - X_2' \partial_{\xi_2} + (1 + \xi_1 X_1'' + \xi_2 X_2'') \partial_\zeta + o(X). \tag{B6}
$$

And the time derivative is

$$
\partial_t = \partial_\tau - \partial_\tau X_1 \partial_{\xi_1} - \partial_\tau X_2 \partial_{\xi_2} + (\xi_1 \partial_\tau X_1' + \xi_2 \partial_\tau X_2') \partial_\zeta + o(X). \tag{B7}
$$

Quadratic and higher-order terms in derivatives of X_i are denoted as $o(X)$.

APPENDIX C: ANSATZ FOR THE SKYRMION STRING

Let us first consider the magnetization distribution in the form

$$
\tilde{\boldsymbol{m}}_{\mathrm{A}}(\xi_1, \xi_2, \zeta) = \sin\theta_0(\rho) \cos\phi_0(\xi_1, \xi_2) \boldsymbol{e}_1(\zeta)
$$

$$
+ \sin\theta_0(\rho) \sin\phi_0(\xi_1, \xi_2) \boldsymbol{e}_2(\zeta)
$$

$$
+ \cos\theta_0(\rho) \boldsymbol{e}_{\mathrm{T}}(\zeta), \tag{C1}
$$

where ξ_1, ξ_2, ζ are curvilinear coordinates introduced in Appendix B. Namely, the coordinates (ξ_1, ξ_2) sweep the plane of perpendicular cross section Π_ζ of the string made in point $\boldsymbol{r} = \boldsymbol{\gamma}(\zeta)$. Here $\theta_0(\rho)$ is the profile of the vertical equilibrium string oriented along the applied magnetic field, and $\rho = \sqrt{\xi_1^2 + \xi_2^2}$. The function $\theta_0(\rho)$ is assumed to be known, and it coincides with the skyrmion profile in a 2D magnet. The angular variable $\phi_0(\xi_1, \xi_2) = \chi + \varphi_0$ determines the magnetization orientation within the plane Π_ζ. Here $\cos\chi = \xi_1/\sqrt{\xi_1^2 + \xi_2^2}$ and $\sin\chi = \xi_2/\sqrt{\xi_1^2 + \xi_2^2}$. In other words, (ρ, χ) are polar coordinates within Π_ζ in the same manner as for a planar skyrmion; see Fig. 12. Constants $\varphi_0 = \pm\pi/2$ and $\varphi_0 = 0, \pi$ for Bloch and Néel skyrmion strings, respectively. An example of the magnetization distribution (C1) for a Bloch string is shown in Fig. 2(a).

So, for a given ζ, model (C1) determines the magnetization within Π_ζ. However, (C1) cannot be used as a string ansatz because it is ambiguous on large distances from the string where different planes Π_ζ for different ζ can intersect. In other words, model (C1) makes sense only for $\rho\kappa \ll 1$, where κ is the string curvature. Moreover, (C1) does not satisfy the required boundary condition $\lim_{\varrho\to\infty} \boldsymbol{m} = \hat{z}$. For this reason,
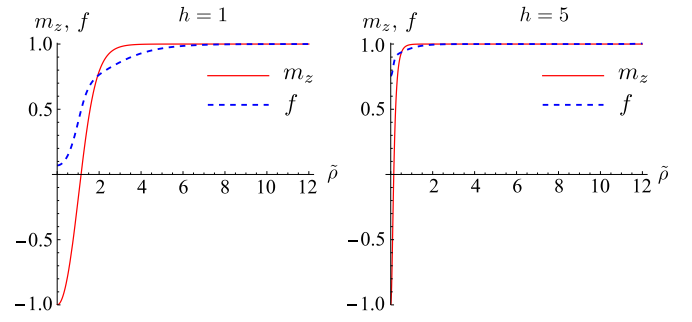

FIG. 13. Functions f obtained as solutions of Eq. (D7) for different values of magnetic field h are compared to the corresponding skyrmion profiles m_z.

we consider the modified ansatz

$$
\boldsymbol{m}_{\mathrm{A}}(\xi_1, \xi_2, \zeta) = \mathfrak{R}_{\boldsymbol{u}}(\alpha_f) \tilde{\boldsymbol{m}}_{\mathrm{A}}(\xi_1, \xi_2, \zeta). \tag{C2}
$$

Here $\mathfrak{R}_{\boldsymbol{u}}(\alpha_f)$ is Rodrigues' rotation matrix

$$
\mathfrak{R}_{\boldsymbol{u}}(\alpha_f) = \cos\alpha_f \, \mathbf{I} + \sin\alpha_f \, [\boldsymbol{u}]_\times + (1 - \cos\alpha_f)(\boldsymbol{u} \otimes \boldsymbol{u}), \tag{C3}
$$

which rotates the vector $\tilde{\boldsymbol{m}}$ around the unit vector $\boldsymbol{u}$ by angle α_f. Here $\mathbf{I}$ is the identity matrix and $[\boldsymbol{u}]_\times$ is the cross-product matrix of $\boldsymbol{u}$. We choose $\boldsymbol{u} = \boldsymbol{e}_{\mathrm{T}} \times \hat{z}/|\boldsymbol{e}_{\mathrm{T}} \times \hat{z}|$ and

$$
\cos\alpha_f = \frac{\sqrt{1 + [1 - f^2(\rho)]|X'|^2}}{\sqrt{1 + |X'|^2}}, \quad \sin\alpha_f = \frac{f(\rho)|X'|}{\sqrt{1 + |X'|^2}}. \tag{C4}
$$

Here function $0 \leqslant f(\rho) \leqslant 1$ controls the magnitude of rotation: the case $f = 0$ corresponds to the absence of rotation, while the case $f = 1$ corresponds to complete rotation by angle $\vartheta_\tau = \angle(\boldsymbol{e}_{\mathrm{T}}, \hat{z})$. The unknown function $f(\rho)$ must have the property $\lim_{\rho\to\infty} f(\rho) = 1$. In the following, we assume that $f^* = 1 - f$ is a localized function whose localization radius ρ^* is much smaller than the curvature radius of the string, i.e., $\rho^*\kappa \ll 1$. A rough estimation of the function $f(\rho)$ is discussed in Appendix D; see Fig. 13.

For $|X'| \ll 1$, the rotation matrix is approximated as

$$
\mathfrak{R}_{\boldsymbol{u}}(\alpha_f) \approx \begin{bmatrix}
1 - \frac{f^2 X_1'^2}{2} & -\frac{f^2 X_1' X_2'}{2} & -f X_1' \\
-\frac{f^2 X_1' X_2'}{2} & 1 - \frac{f^2 X_2'^2}{2} & -f X_2' \\
f X_1' & f X_2' & 1 - \frac{f^2 |X'|^2}{2}
\end{bmatrix}. \tag{C5}
$$

An example of model (C2) is shown in Fig. 2(b).

APPENDIX D: MAGNETIC ENERGIES OF THE STRING

In this Appendix, we compute the contribution from each energy term separately. The exchange interaction is

$$
H_{ex} = A \iiint dx\,dy\,dz (\partial_i \boldsymbol{m} \cdot \partial_i \boldsymbol{m})
$$

$$
= A \int d\zeta \iint d\xi_1 d\xi_2 |J|(\partial_i \boldsymbol{m}_{\mathrm{A}} \cdot \partial_i \boldsymbol{m}_{\mathrm{A}}), \tag{D1}
$$

where $i \in \{x, y, z\}$ are Cartesian coordinates. For $\boldsymbol{m}_{\mathrm{A}}$ we use ansatz (C2) for the case $\theta_0(0) = \pi$ and $\theta_0(\infty) = 0$. The Jacobian $|J|$ is determined from (B4). For the derivatives

∂_i we use (B6) with a sufficient number of terms. Finally, straightforward calculation enables us to write (D1) in the form

$$H_{\text{ex}} = 8\pi A Q^{-1} \int d\tilde{\xi}\,(\mathscr{H}_{\text{ex}}^{(0)} + \mathscr{H}_{\text{ex}}^{(2)} + \mathscr{H}_{\text{ex}}^{(4)} + \cdots),$$

$$\mathscr{H}_{\text{ex}}^{(0)} = c_0,$$

$$\mathscr{H}_{\text{ex}}^{(2)} = \frac{c_0 + \tilde{c}_0}{2}|\mathfrak{X}'|^2 + \frac{c_1}{2}\sin\varphi_0[\mathfrak{X}' \times \mathfrak{X}'']_z + \frac{c_2}{2}|\mathfrak{X}''|^2,$$

$$\mathscr{H}_{\text{ex}}^{(4)} = -\frac{\frac{1}{2}c_0 + \bar{c}_0}{4}|\mathfrak{X}'|^4 - \frac{c_3}{4}\sin\varphi_0|\,\mathfrak{X}'|^2[\,\mathfrak{X}' \times \mathfrak{X}'']_z.$$

Here $\mathfrak{X} = QX$, $\tilde{\xi} = Q\zeta$ with $Q = D/(2A)$, and $\mathfrak{X}' = \partial_{\tilde{\xi}}\mathfrak{X}$. The coefficients are functionals of $\theta_0(\tilde{\rho})$ and $f(\tilde{\rho})$:

$$c_0 = \frac{1}{4}\int_0^\infty \left[\theta_0'^2 + \frac{\sin^2\theta_0}{\tilde{\rho}^2}\right]\tilde{\rho}\,d\tilde{\rho},$$

$$\tilde{c}_0 = \frac{1}{4}\int_0^\infty f'^2(1 + \cos^2\theta_0)\tilde{\rho}\,d\tilde{\rho},$$

$$c_1 = -\frac{1}{2}\int_0^\infty \tilde{\rho}^2\theta_0'f'\,d\tilde{\rho},$$

$$c_2 = \frac{1}{4}\int_0^\infty \tilde{\rho}(1 + \cos^2\theta_0)(1 - f)^2 d\tilde{\rho},$$

$$\bar{c}_0 = \frac{1}{4}\int_0^\infty \tilde{\rho}(1 + \cos^2\theta_0)f'^2(1 - 2f^2)d\tilde{\rho},$$

$$c_3 = -\frac{1}{2}\int_0^\infty \tilde{\rho}^2\theta_0'f'(2 - f^2)d\tilde{\rho},$$

where $\tilde{\rho} = Q\rho$, $\theta_0' = \partial_{\tilde{\rho}}\theta_0$ and $f' = \partial_{\tilde{\rho}}f$. Note the absence of the cubic nonlinear term.

In an analogous manner, we determine the energy of DMI:

$$H_{\text{DMI}} = D\int d\zeta \iint d\xi_1 d\xi_2 |J|\,\boldsymbol{m}_{\text{A}} \cdot [\boldsymbol{\nabla} \times \boldsymbol{m}_{\text{A}}]$$

$$= 8\pi DQ^{-2}\int d\tilde{\xi}\,(\mathscr{H}_{\text{DMI}}^{(0)} + \mathscr{H}_{\text{DMI}}^{(2)} + \mathscr{H}_{\text{DMI}}^{(4)} + \cdots).$$

Here $\mathscr{H}_{\text{DMI}}^{(0)} = \frac{1}{4}\sin\varphi_0\int_0^\infty \mathscr{E}_{\text{DMI}}(\tilde{\rho})\tilde{\rho}\,d\tilde{\rho} = \text{const}$ with $\mathscr{E}_{\text{DMI}} = \theta_0' + \frac{1}{\tilde{\rho}}\sin\theta_0\cos\theta_0$ represents DMI energy density of the vertical equilibrium string. The higher-order terms are as follows:

$$\mathscr{H}_{\text{DMI}}^{(2)} = \frac{c_6}{2}\sin\varphi_0|\mathfrak{X}'|^2 + \frac{c_7}{2}[\mathfrak{X}' \times \mathfrak{X}'']_z,$$

$$\mathscr{H}_{\text{DMI}}^{(4)} = -\frac{c_8}{4}\sin\varphi_0|\mathfrak{X}'|^4 - \frac{c_9}{4}|\mathfrak{X}'|^2[\mathfrak{X}' \times \mathfrak{X}'']_z.$$

Note that the cubic terms are absent, similar to the case of the exchange energy. The coefficients have the following form:

$$c_6 = \frac{1}{8}[(2 - f^2)\mathscr{E}_{\text{DMI}} + ff'\sin 2\theta_0]\tilde{\rho}d\tilde{\rho},$$

$$c_7 = -\frac{1}{2}\int_0^\infty d\tilde{\rho}\tilde{\rho}(1 - f)[1 - f\cos^2\theta_0],$$

$$c_8 = \frac{1}{16}\int_0^\infty d\tilde{\rho}\tilde{\rho}\big[\mathscr{E}_{\text{DMI}}\big(1 + (1 - f^2)^2\big)$$

$$+ 2\sin 2\theta_0 f'f(1 - f^2)\big],$$

$$c_9 = -\frac{1}{4}\int_0^\infty d\tilde{\rho}\tilde{\rho}\Bigg[\sin^2\theta_0\left(1 - f^3 + \frac{1}{2}f^4\right)$$

$$- 2f(1 - f)(2 - f)$$

$$- \tilde{\rho}f'\left(2 - f^2 + \frac{1}{4}f^2\sin^2\theta_0\right)\Bigg].$$

For Zeeman energy, we obtain the analogous series

$$H_z = M_s\mu_0 H_{\text{ext}}\int d\zeta \iint d\xi_1 d\xi_2 |J|(1 - m_{\text{A}z})$$

$$= 8\pi M_s\mu_0 H_{\text{ext}}Q^{-3}$$

$$\times \int d\tilde{\xi}\,(\mathscr{H}_z^{(0)} + \mathscr{H}_z^{(2)} + \mathscr{H}_z^{(4)} + \cdots),$$

$$\mathscr{H}_z^{(0)} = \frac{1}{4}\int_0^\infty (1 - \cos\theta_0)\tilde{\rho}\,d\tilde{\rho},$$

$$\mathscr{H}_z^{(2)} = \frac{c_{10}}{2}|\mathfrak{X}'|^2 + \frac{c_{11}}{2}\sin\varphi_0[\mathfrak{X}' \times \mathfrak{X}'']_z,$$

$$\mathscr{H}_z^{(4)} = -\frac{c_{12}}{4}|\mathfrak{X}'|^4 - \frac{c_{13}}{4}\sin\varphi_0|\mathfrak{X}'|^2[\mathfrak{X}' \times \mathfrak{X}'']_z,$$

with the coefficients

$$c_{10} = \frac{1}{4}\int_0^\infty d\tilde{\rho}\tilde{\rho}[1 - \cos\theta_0 f(2 - f)],$$

$$c_{11} = \frac{1}{4}\int_0^\infty d\tilde{\rho}\tilde{\rho}^2(1 - f)\sin\theta_0,$$

$$c_{12} = \frac{1}{8}\int_0^\infty d\tilde{\rho}\tilde{\rho}[1 - \cos\theta_0 f(4 - 4f + f^3)],$$

$$c_{13} = -\frac{1}{4}\int_0^\infty d\tilde{\rho}\tilde{\rho}^2 f(1 - f)\sin\theta_0.$$

Collecting all energy terms together, we write the harmonic and nonlinear parts of the total longitudinal energy densities in the form of (7) with the following harmonic and leading nonlinear terms:

$$\mathscr{H}^{(2)} = \frac{a_1}{2}|\mathfrak{X}'|^2 + \frac{a_2}{2}\sigma[\mathfrak{X}' \times \mathfrak{X}'']_z + \frac{a_3}{2}|\mathfrak{X}''|^2 + \cdots,$$

$$\mathscr{H}^{(4)} = -\frac{b_1}{4}|\mathfrak{X}'|^4 - \frac{b_2}{4}\sigma|\mathfrak{X}'|^2[\mathfrak{X}' \times \mathfrak{X}'']_z + \cdots,$$

$$(D5)$$

where $\sigma = \sin\varphi_0 = \pm 1$. For the chosen boundary conditions for θ_0, we have $\sigma = \text{sgn}(D)$. Since $\tilde{\xi} = \tilde{z}$ on the string, we replace $\tilde{\xi} \to \tilde{z}$ in the integral (7). In terms of ψ, Eqs. (D5) have the form of Eqs. (8). The coefficients are as follows:

$$a_1 = c_0 + \tilde{c}_0 + 2c_6 + 2hc_{10}, \qquad (D6a)$$

$$a_2 = c_1 + 2c_7 + 2hc_{11}, \quad a_3 = c_2,$$

$$b_1 = \frac{c_0}{2} + \bar{c}_0 + 2c_8 + 2hc_{12},$$

$$b_2 = c_3 + 2c_9 + 2hc_{13}. \qquad (D6b)$$

The function $f(\tilde{\rho})$ which determines the coefficients a_n and b_n is unknown. However, it can be roughly estimated in the limit of the long-wave approximation, where the term $\frac{1}{2}a_1|X'|^2$ gives the main contribution to the energy. This enables us to estimate the function $f(\tilde{\rho})$ as a minimizer of the coefficient a_1 which is a functional of $f(\tilde{\rho})$. The equa-
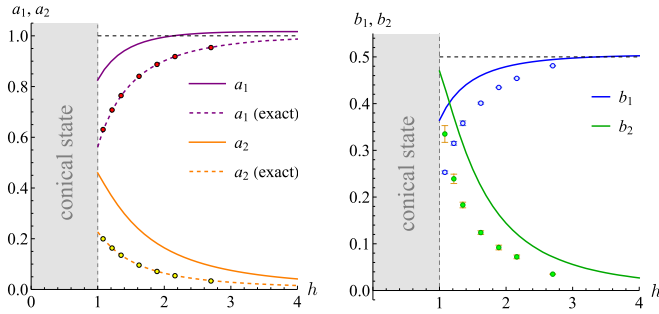
FIG. 14. Field dependence of the first two coefficients of the linear (a_1, a_2) and nonlinear (b_1, b_2) parts of the Hamiltonian of the Bloch skyrmion string. Solid lines correspond to expressions (D6a) and (D6b) with the use of function f estimated as a solution of Eq. (D7). Dashed lines correspond to the exact values of a_1 and a_2 previously obtained from the linear dispersion of the translational magnon mode [45]. Dots show the corresponding coefficients determined numerically from micromagnetic simulations; for detail, see Appendix F.

tion $\delta a_1 / \delta f = 0$ has the following explicit form:

$$
\begin{aligned}
f'' &+ \left[\frac{1}{\tilde{\rho}} - \theta_0' \frac{\sin 2\theta_0}{1 + \cos^2 \theta_0} \right] f' + \frac{2b \cos \theta_0}{1 + \cos^2 \theta_0} (1 - f) \\
&+ 2f \frac{\theta_0' \cos^2 \theta_0 + \frac{1}{\tilde{\rho}} \sin \theta_0 \cos \theta_0}{1 + \cos^2 \theta_0} = 0.
\end{aligned} \tag{D7}
$$

Equation (D7) is supplemented with the boundary conditions $f'(0) = 0$ and $f(\infty) = 1$. Some solutions for different skyrmion profiles are shown in Fig. 13. An important consequence of the obtained solution is $f(0) \neq 0$. This means that the magnetization in the string center is not tangential to the string. In the limit $h \to \infty$, we obtain $f(0) \to 1$. This means that the magnetization of the string center is antiparallel to the applied field for the infinitely thin string. From Fig. 13, one can conclude that function f possesses two lengthscales: one corresponds to the exponential localization within the skyrmion core, and the other corresponds to a longer range decay. The latter indicates that not only are the spins of the skyrmion core involved in the string deformation, but also some halo of spins some distance from the core.

In the large-field limit we have $f \approx 1$, and from the form of the coefficients c we conclude that the contributions of all energies vanish except the exchange energy. In this case, $c_0 \to 1$ and therefore $a_1 \to 1$ and $b_1 \to 1/2$.

Having function f, we estimate the coefficients a_i and b_i; see Fig. 14. A comparison with the corresponding coefficients obtained by means of micromagnetic simulations shows that the considered model and the estimation of function f by means of Eq. (D7) result in qualitative agreement with the real dependencies $a_n(h)$ and $b_n(h)$. The best agreement is achieved for the case of large fields which correspond to thin strings. The quantitative analysis should be based on the values of a_n and b_n determined by means of micromagnetic simulation; see Appendix F.

APPENDIX E: DETAILS OF MICROMAGNETIC SIMULATIONS

Simulation of the dynamics of the magnetization media is based on the numerical solution of the Landau-Lifshitz equation,

$$
\partial_t \boldsymbol{m} = -\gamma_0' [\boldsymbol{m} \times \boldsymbol{B}_{\text{eff}}] - \gamma_0' \alpha_{\text{G}} [\boldsymbol{m} \times (\boldsymbol{m} \times \boldsymbol{B}_{\text{eff}})], \tag{E1}
$$

where $\gamma_0' = \gamma_0 / (1 + \alpha_{\text{G}}^2)$, with α_{G} being the Gilbert damping, and $\boldsymbol{B}_{\text{eff}} = -\frac{1}{M_s} \frac{\delta H}{\delta \boldsymbol{m}}$ is the effective field. The solution is performed by means of the mumax³ code [75]. We consider Hamiltonian (6) with the material parameters of FeGe, namely $A = 8.78$ pJ/m, $D = 1.58$ mJ/m², $M_s = 0.384$ MA/m. The scales of the length and time are determined by the wave vector $Q = D/(2A) \approx 2\pi/(70 \text{ nm})$ and frequency $\omega_{c2} = \gamma_0 D^2 / (2AM_s) \approx 10.4$ GHz, respectively. The corresponding saturation field is $B_0 = \omega_{c2}/\gamma_0 \approx 0.37$ T. The discretization mesh $\Delta x \times \Delta y \times \Delta z$ with $\Delta x = \Delta y = \Delta z = 1$ nm was used in most of the simulations, except for the case of the breather, where we used $\Delta x = \Delta y = 0.5$ nm. The simulated samples have the form of a cuboid with sizes $L_x \times L_y \times L_z$ and with periodic boundary conditions applied in all three directions. The transversal size is in the range $L_x = L_y = 100$–140 nm; for smaller fields (thicker strings), we use samples of larger lateral size. The size L_z along the applied magnetic field is different for the different simulations, as is indicated in the corresponding figures.

APPENDIX F: DETERMINATION OF THE COEFFICIENTS a_n AND b_n BY MEANS OF MICROMAGNETIC SIMULATIONS

To determine the coefficients a_n and b_n, we simulated a damping-free dynamics of helical waves for different values of the helix radius $\mathcal{R}$ and wave vector k_0. For each simulation, we determine the frequency of the helix rotation $\omega = \omega(k_0, \mathcal{R})$. Based on the knowledge of the form of nonlinear dispersion (11), we extract coefficients a_n and b_n as explained below.

It is important to note that the coefficients a_n and b_n are defined for the dimensionless dispersion (11), thus they depend on a single parameter h only. This means that the dependencies $a_n(h)$ and $b_n(h)$ extracted from simulations are universal, i.e., they are valid for any cubic chiral magnet, not only FeGe.

For a given value of k_0 we programmatically prepare an initial state close to a helix solution (10) with radius approximately 10 nm. The sample length $L_z = 2\pi/(|k_0|Q)$ is equal to the helix period, and the periodic boundary conditions are applied in all three directions. At the first step, we simulate the overdamped dynamics ($\alpha_{\text{G}} = 0.5$) until the string reaches its equilibrium state in the form of a vertical rectilinear line. During this overdamped dynamics, we save several dozen of the magnetization snapshots. In this manner, we obtain the helical waves of different radii in the range 1–8 nm. At the next step, we use these configurations as the initial states for the damping-free simulation of the helical wave dynamics. Using definition (1), we extract the string central line $\boldsymbol{X}(\tilde{z}, \tilde{t})$. For a fixed horizontal cross section $\tilde{z} = \tilde{z}_0$, the linear time dependence of the phase $\arg (X_1(\tilde{z}_0, \tilde{t}) + iX_2(\tilde{z}_0, \tilde{t})) = -\omega \tilde{t}$
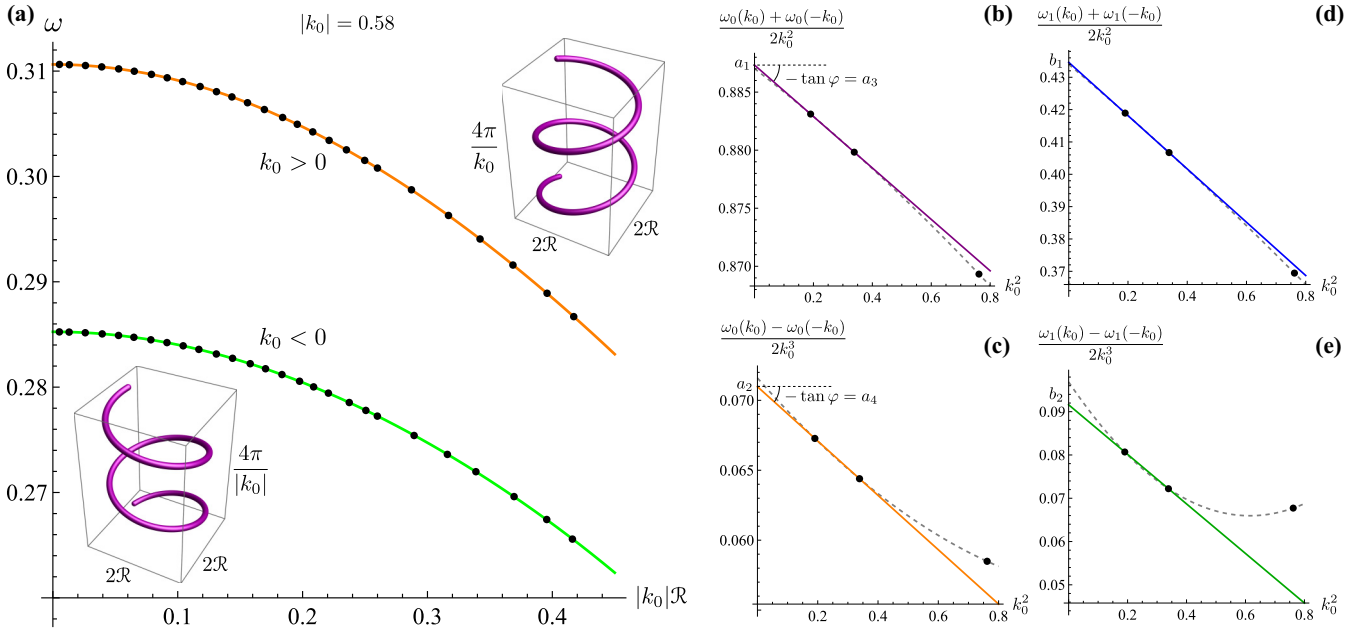
FIG. 15. Determination of the coefficients a_n and b_n for the case $h = 1.89$ (0.7 T). Panel (a) shows the amplitude dependence of the helical wave frequency obtained by means of micromagnetic simulations for the wave vector $k_0 = 0.58$ ($\frac{2\pi}{120\,\text{nm}}$). Solid lines correspond to the fitting $\omega = \omega_0 - \omega_1 \mathcal{R}^2 k_0^2 + \omega_2 \mathcal{R}^4 k_0^4 + \omega_3 \mathcal{R}^6 k_0^6$. Next, the fitting coefficients ω_n are determined for several additional values of k_0, namely $k_0 = 0.44$ ($\frac{2\pi}{160\,\text{nm}}$) and $k_0 = 0.87$ ($\frac{2\pi}{80\,\text{nm}}$). The linear extrapolation of the dependence $[\omega_0(k_0) + \omega_0(-k_0)]/(2k_0^2)$ on k_0^2 to the region of vanishing k_0 enables one to determine coefficients a_1 and a_3; see panel (b) and the corresponding explanations in the text. Similarly, we determine coefficients a_2 and a_4 using the dependence $[\omega_0(k_0) - \omega_0(-k_0)]/(2k_0^3)$ on k_0^2; see panel (c). The parabolic extrapolation based on three points (dashed line) is used for the error bars estimation. Coefficients b_n are determined analogously after the replacement $\omega_0 \rightarrow \omega_1$; see the insets (d) and (e).

enables us to extract the frequency ω. As an example, in Fig. 15 we demonstrate the values of ω obtained for different helix radii and two different signs of k_0.

Performing the interpolation $\omega = \omega_0 - \omega_1 \mathcal{R}^2 k_0^2 + \omega_2 \mathcal{R}^4 k_0^4 + \omega_3 \mathcal{R}^6 k_0^6$, we determine the coefficients ω_n. Repeating the above-described procedure for various k_0, we determine numerically the dependence $\omega_n(k_0)$. Since $\omega_0(k_0) = a_1 k_0^2 + a_2 k_0^3 + a_3 k_0^4 + \cdots$, one can write $[\omega_0(k_0) + \omega_0(-k_0)]/(2k_0^2) = a_1 + a_3 k_0^2 + \cdots$. This enables us to determine the coefficients a_1 and a_3 as explained in Fig. 15(b). Similarly, we determine the coefficients a_2 and a_3 using that $[\omega_0(k_0) - \omega_0(-k_0)]/(2k_0^3) = a_2 + a_4 k_0^2 + \cdots$; see Fig. 15(c). Coefficients b_n are determined analogously, but with the replacement $\omega_0(k_0) \rightarrow \omega_1(k_0)$; see Figs. 15(d) and 15(e). Coefficients a_n and b_n determined by this method for various fields are shown in Figs. 4 and 14. Note that the practically achievable accuracy of simulations does not allow us to determine the higher nonlinear coefficients $b_{n>2}$ with acceptable precision.

APPENDIX G: METHOD OF MULTIPLE SCALES

Here we adapt to our case the derivation presented in Ref. [46]. We will look for a solution of (9) in the form

$$\psi = \sum_{i=1}^{\infty} u_i \varepsilon^i, \tag{G1}$$

where ε is a small parameter, and $u_i = u_i(Z_0, Z_1, \ldots, T_0, T_1, \ldots)$ are functions of many space

and time variables of different scales, namely $Z_i = \tilde{z}\varepsilon^i$ and $T_i = \tilde{t}\varepsilon^i$ with $i = 0, 1, \ldots$. Thus $Z_0 = \tilde{z}$ and $T_0 = \tilde{t}$.

Now we substitute (G1) into (9) and take into account the form of the derivatives $\partial_{\tilde{z}} = \varepsilon^i \partial_{Z_i}$ and $\partial_{\tilde{t}} = \varepsilon^i \partial_{T_i}$ where the summation over i is assumed. Collecting only terms linear in ε, we obtain

$$\hat{\mathbb{L}} u_1 = 0,$$
$$\hat{\mathbb{L}} = i\partial_{T_0} + a_1 \partial_{Z_0}^2 - i a_2 \partial_{Z_0}^3 - a_3 \partial_{Z_0}^4 + \cdots, \tag{G2}$$

whose solution is $u_1 = \tilde{\mathcal{A}}(Z_1, Z_2, \ldots, T_1, T_2)e^{i\theta}$, where $\theta = k_0 Z_0 - \omega_0(k_0)T_0$. Here the complex-valued function $\tilde{\mathcal{A}}$ describes the slowly varying amplitude of the envelope wave, and ω_0 is the linear part of the dispersion introduced in (11b).

Collecting now terms proportional to ε^2, we obtain

$$\hat{\mathbb{L}} u_2 = -i[\partial_{T_1}\mathcal{A} + v_g(k_0)\partial_{Z_1}\mathcal{A}]e^{i\theta}, \tag{G3}$$

where $v_g = \partial_k \omega_0$ is the group velocity of the linear wave. The inhomogeneous equation (G3) has bounded solutions (without secular terms) for u_2 if the right-hand side of Eq. (G3) is orthogonal to solutions of the corresponding homogeneous equation. This means that $\partial_{T_1}\tilde{\mathcal{A}} + v_g(k_0)\partial_{Z_1}\tilde{\mathcal{A}} = 0$. Thus, in the first approximation, the envelope $\tilde{\mathcal{A}}$ moves with the group velocity. In other words, $\tilde{\mathcal{A}} = \tilde{\mathcal{A}}(Z_1 - v_g(k_0)T_1; Z_2, \ldots, T_2, \ldots)$. In this case, Eq. (G3) obtains the homogeneous form $\hat{\mathbb{L}} u_2 = 0$, which allows the trivial solution $u_2 = 0$.

Collecting now terms proportional to ε^3, we obtain

$$\hat{\mathbb{L}}u_3 = -\Big\{i[\partial_{T_2}\tilde{\mathcal{A}} + v_g(k_0)\partial_{Z_2}\tilde{\mathcal{A}}] + \frac{\mu(k_0)}{2}\partial_{Z_1}^2\tilde{\mathcal{A}}$$

$$+ \nu(k_0)\tilde{\mathcal{A}}|\tilde{\mathcal{A}}|^2\Big\}e^{i\theta}, \qquad \text{(G4)}$$

where $\mu(k_0)$ and $\nu(k_0)$ are the same as in (14). The condition of absence of the secular terms in the solution for u_3 requires the vanishing curly brackets on the right-hand side of Eq. (G4). The latter results in NLSE (14), where we made the substitution $\tilde{\mathcal{A}} = \varepsilon\mathcal{A}$.

APPENDIX H: GENERAL EQUATION OF THE COLLECTIVE STRING DYNAMICS

It is convenient to proceed to the angular parametrization of the magnetization $\boldsymbol{m} = \sin\theta(\cos\phi\hat{\boldsymbol{x}} + \sin\phi\hat{\boldsymbol{y}}) + \cos\theta\hat{\boldsymbol{z}}$. In this case, the Lagrangian and the density of the dissipative function are

$$\mathcal{L} = \frac{M_s}{\gamma_0}\iint(1 - \cos\theta)\dot{\phi}\,dxdy - \mathcal{H}, \qquad \text{(H1a)}$$

$$\mathcal{F} = \frac{\alpha}{2}\frac{M_s}{\gamma_0}\iint(\dot{\theta}^2 + \sin^2\theta\dot{\phi}^2)dxdy. \qquad \text{(H1b)}$$

Now we assume that $\theta = \theta_0(x, y, X_i(z, t), X_i'(z, t))$ and $\phi = \phi_0(x, y, X_i(z, t), X_i'(z, t))$, with θ_0 and ϕ_0 being the known functions. Taking into account that

$$\dot{\phi} = \frac{\partial\phi_0}{\partial X_i}\dot{X}_i + \frac{\partial\phi_0}{\partial X_i'}\dot{X}_i', \quad \phi' = \frac{\partial\phi_0}{\partial X_i}X_i' + \frac{\partial\phi_0}{\partial X_i'}X_i'',$$

$$\dot{\theta} = \frac{\partial\theta_0}{\partial X_i}\dot{X}_i + \frac{\partial\theta_0}{\partial X_i'}\dot{X}_i', \quad \theta' = \frac{\partial\theta_0}{\partial X_i}X_i' + \frac{\partial\theta_0}{\partial X_i'}X_i'', \qquad \text{(H2)}$$

we write the general equations of motion $\delta\mathfrak{S}/\delta X_i = \delta\mathfrak{F}/\delta\dot{X}_i$ in the form (22), where

$$G_{ij}^{(0)} = \frac{M_s}{\gamma_0}\iint\sin\theta_0\left[\frac{\partial\theta_0}{\partial X_i}\frac{\partial\phi_0}{\partial X_j} - \frac{\partial\theta_0}{\partial X_j}\frac{\partial\phi_0}{\partial X_i}\right]dxdy,$$

$$G_{ij}^{(1)} = \frac{M_s}{\gamma_0}\iint\sin\theta_0\left[\frac{\partial\theta_0}{\partial X_i}\frac{\partial\phi_0}{\partial X_j'} - \frac{\partial\theta_0}{\partial X_j'}\frac{\partial\phi_0}{\partial X_i}\right]dxdy,$$

$$G_{ij}^{(2)} = \frac{M_s}{\gamma_0}\iint\sin\theta_0\left[\frac{\partial\theta_0}{\partial X_i'}\frac{\partial\phi_0}{\partial X_j'} - \frac{\partial\theta_0}{\partial X_j'}\frac{\partial\phi_0}{\partial X_i'}\right]dxdy \qquad \text{(H3)}$$

are the gyrotensors, and

$$D_{ij}^{(0)} = \frac{M_s}{\gamma_0}\iint\left[\frac{\partial\theta_0}{\partial X_i}\frac{\partial\theta_0}{\partial X_j} + \sin^2\theta_0\frac{\partial\phi_0}{\partial X_i}\frac{\partial\phi_0}{\partial X_j}\right]dxdy,$$

$$D_{ij}^{(1)} = \frac{M_s}{\gamma_0}\iint\left[\frac{\partial\theta_0}{\partial X_i}\frac{\partial\theta_0}{\partial X_j'} + \sin^2\theta_0\frac{\partial\phi_0}{\partial X_i}\frac{\partial\phi_0}{\partial X_j'}\right]dxdy,$$

$$D_{ij}^{(2)} = \frac{M_s}{\gamma_0}\iint\left[\frac{\partial\theta_0}{\partial X_i'}\frac{\partial\theta_0}{\partial X_j'} + \sin^2\theta_0\frac{\partial\phi_0}{\partial X_i'}\frac{\partial\phi_0}{\partial X_j'}\right]dxdy \qquad \text{(H4)}$$

are the damping tensors. Note that due to the presence of terms with the mixed derivatives $\dot{X}_i'$ in (H2), it is required to work with the action, not with the Lagrange function.

APPENDIX I: DESCRIPTION OF THE SUPPLEMENTAL MOVIES

Movies 1 and 2 are the dynamical realization of Fig. 5 for the cases $k > 0$ and $k < 0$, respectively. All parameters and notations are the same as indicated in the caption of Fig. 5.

Movie 3 demonstrates the dynamics of the dn-cnoidal wave shown in Fig. 7(a) in the time interval $t \in [10T - 15T] = [5.06 - 7.6]$ ns.

Movie 4 demonstrates the dynamics of the cn-cnoidal wave shown in Fig. 7(b) in the time interval $t \in [10T - 15T] = [3.78 - 5.7]$ ns. The parameters and notations are the same as in Fig. 7.

Movie 5 shows the propagation of the soliton shown in Fig. 8 along the string. The parameters and notations are the same as in Fig. 8.

Movie 6 shows the propagation of Ma-breather shown in Fig. 9 along the string. The parameters and notations are the same as in Fig. 9.

[1] S. Seki and M. Mochizuki, in *Skyrmions in Magnetic Materials*, 1st ed. (Springer, Cham, 2016), p. 69. (2016).

[2] J. P. Liu, Z. Zhang, and G. Zhao, *Skyrmions. Topological Structures, Properties, and Applications* (CRC, Boca Raton, FL, 2020).

[3] C. Back, V. Cros, H. Ebert, K. Everschor-Sitte, A. Fert, M. Garst, T. Ma, S. Mankovsky, T. L. Monchesky, M. Mostovoy, N. Nagaosa, S. S. P. Parkin, C. Pfleiderer, N. Reyren, A. Rosch, Y. Taguchi, Y. Tokura, K. von Bergmann, and J. Zang, The 2020 skyrmionics roadmap, J. Phys. D **53**, 363001 (2020).

[4] N. Nagaosa and Y. Tokura, Topological properties and dynamics of magnetic skyrmions, Nat. Nanotechnol. **8**, 899 (2013).

[5] A. Fert, N. Reyren, and V. Cros, Magnetic skyrmions: advances in physics and potential applications, Nat. Rev. Mater. **2**, 17031 (2017).

[6] R. Wiesendanger, Nanoscale magnetic skyrmions in metallic films and multilayers: A new twist for spintronics, Nat. Rev. Mater. **1**, 16044 (2016).

[7] A. N. Bogdanov and C. Panagopoulos, Physical foundations and basic properties of magnetic skyrmions, Nat. Rev. Phys. **2**, 492 (2020).

[8] J. Sampaio, V. Cros, S. Rohart, A. Thiaville, and A. Fert, Nucleation, stability and current-induced motion of isolated magnetic skyrmions in nanostructures, Nat. Nanotechnol. **8**, 839 (2013).

[9] X. Zhang, M. Ezawa, and Y. Zhou, Magnetic skyrmion logic gates: Conversion, duplication and merging of skyrmions, Sci. Rep. **5**, 9400 (2015).

[10] A. Fert, V. Cros, and J. Sampaio, Skyrmions on the track, Nat. Nanotechnol. **8**, 152 (2013).

[11] S. Mühlbauer, B. Binz, F. Jonietz, C. Pfleiderer, A. Rosch, A. Neubauer, R. Georgii, and P. Böni, Skyrmion lattice in a chiral magnet, Science **323**, 915 (2009).

[12] S. Seki, M. Suzuki, M. Ishibashi, R. Takagi, N. D. Khanh, Y. Shiota, K. Shibata, W. Koshibae, Y. Tokura, and T. Ono, Direct visualization of the three-dimensional shape of skyrmion strings in a noncentrosymmetric magnet, Nat. Mater. **21**, 181 (2022).

[13] M. T. Birch, D. Cortés-Ortuño, L. A. Turnbull, M. N. Wilson, F. Groß, N. Träger, A. Laurenson, N. Bukin, S. H. Moody, M. Weigand, G. Schütz, H. Popescu, R. Fan, P. Steadman, J. A. T. Verezhak, G. Balakrishnan, J. C. Loudon, A. C. Twitchett-Harrison, O. Hovorka, H. Fangohr *et al.*, Real-space imaging of confined magnetic skyrmion tubes, Nat. Commun. **11**, 1726 (2020).

[14] D. Wolf, S. Schneider, U. K. Rößler, A. Kovács, M. Schmidt, R. E. Dunin-Borkowski, B. Büchner, B. Rellinghaus, and A. Lubk, Unveiling the three-dimensional magnetic texture of skyrmion tubes, Nat. Nanotechnol. **17**, 250 (2022).

[15] L. M. Pismen, *Vortices in Nonlinear Field*, edited by J. Birman (Oxford University Press, New York, 1999).

[16] E. B. Sonin, Vortex oscillations and hydrodynamics of rotating superfluids, Rev. Mod. Phys. **59**, 87 (1987).

[17] G. Blatter, M. V. Feigel'man, V. B. Geshkenbein, A. I. Larkin, and V. M. Vinokur, Vortices in high-temperature superconductors, Rev. Mod. Phys. **66**, 1125 (1994).

[18] K. W. Madison, F. Chevy, W. Wohlleben, and J. Dalibard, Vortex formation in a stirred Bose-Einstein condensate, Phys. Rev. Lett. **84**, 806 (2000).

[19] T. Schulz, R. Ritz, A. Bauer, M. Halder, M. Wagner, C. Franz, C. Pfleiderer, K. Everschor, M. Garst, and A. Rosch, Emergent electrodynamics of skyrmions in a chiral magnet, Nat. Phys. **8**, 301 (2012).

[20] P. Bruno, V. K. Dugaev, and M. Taillefumier, Topological Hall effect and Berry phase in magnetic nanostructures, Phys. Rev. Lett. **93**, 096806 (2004).

[21] S.-Z. Lin and A. Saxena, Dynamics of Dirac strings and monopolelike excitations in chiral magnets under a current drive, Phys. Rev. B **93**, 060401(R) (2016).

[22] H.-B. Braun, Topological effects in nanomagnetism: From superparamagnetism to chiral quantum solitons, Adv. Phys. **61**, 1 (2012).

[23] P. Milde, D. Kohler, J. Seidel, L. M. Eng, A. Bauer, A. Chacon, J. Kindervater, S. Muhlbauer, C. Pfleiderer, S. Buhrandt *et al.*, Unwinding of a skyrmion lattice by magnetic monopoles, Science **340**, 1076 (2013).

[24] C. Schütte and A. Rosch, Dynamics and energetics of emergent magnetic monopoles in chiral magnets, Phys. Rev. B **90**, 174432 (2014).

[25] S. Seki, M. Garst, J. Waizner, R. Takagi, N. D. Khanh, Y. Okamura, K. Kondou, F. Kagawa, Y. Otani, and Y. Tokura, Propagation dynamics of spin excitations along skyrmion strings, Nat. Commun. **11**, 256 (2020).

[26] X. Xing, Y. Zhou, and H. B. Braun, Magnetic skyrmion tubes as nonplanar magnonic waveguides, Phys. Rev. Appl. **13**, 034051 (2020).

[27] N. Mathur, F. S. Yasin, M. J. Stolt, T. Nagai, K. Kimoto, H. Du, M. Tian, Y. Tokura, X. Yu, and S. Jin, In-plane magnetic field-driven creation and annihilation of magnetic skyrmion strings in nanostructures, Adv. Funct. Mater. **31**, 2008521 (2021).

[28] M. T. Birch, D. Cortés-Ortuño, K. Litzius, S. Wintz, F. Schulz, M. Weigand, A. Štefančič, D. A. Mayoh, G. Balakrishnan, P. D. Hatton, and G. Schütz, Toggle-like current-induced bloch point dynamics of 3D skyrmion strings in a room temperature nanowire, Nat. Commun. **13**, 3630 (2022).

[29] T. Yokouchi, S. Hoshino, N. Kanazawa, A. Kikkawa, D. Morikawa, K. Shibata, T. hisa Arima, Y. Taguchi, F. Kagawa, N. Nagaosa, and Y. Tokura, Current-induced dynamics of skyrmion strings, Sci. Adv. **4**, eaat1115 (2018).

[30] F. Jonietz, S. Muhlbauer, C. Pfleiderer, A. Neubauer, W. Munzer, A. Bauer, T. Adams, R. Georgii, P. Boni, R. A. Duine, K. Everschor, M. Garst, and A. Rosch, Spin transfer torques in MnSi at ultralow current densities, Science **330**, 1648 (2010).

[31] X. Yu, N. Kanazawa, W. Zhang, T. Nagai, T. Hara, K. Kimoto, Y. Matsui, Y. Onose, and Y. Tokura, Skyrmion flow near room temperature in an ultralow current density, Nat. Commun. **3**, 988 (2012).

[32] J. Tang, Y. Wu, W. Wang, L. Kong, B. Lv, W. Wei, J. Zang, M. Tian, and H. Du, Magnetic skyrmion bundles and their current-driven dynamics, Nat. Nanotechnol. **16**, 1086 (2021).

[33] S. Okumura, V. P. Kravchuk, and M. Garst, Instability of magnetic skyrmion strings induced by longitudinal spin currents, Phys. Rev. Lett. **131**, 066702 (2023).

[34] F. Kagawa, H. Oike, W. Koshibae, A. Kikkawa, Y. Okamura, Y. Taguchi, N. Nagaosa, and Y. Tokura, Current-induced viscoelastic topological unwinding of metastable skyrmion strings, Nat. Commun. **8**, 1332 (2017).

[35] X. Yu, J. Masell, F. S. Yasin, K. Karube, N. Kanazawa, K. Nakajima, T. Nagai, K. Kimoto, W. Koshibae, Y. Taguchi, N. Nagaosa, and Y. Tokura, Real-space observation of topological defects in extended skyrmion-strings, Nano Lett. **20**, 7313 (2020).

[36] J. Xia, X. Zhang, O. A. Tretiakov, H. T. Diep, J. Yang, G. Zhao, M. Ezawa, Y. Zhou, and X. Liu, Bifurcation of a topological skyrmion string, Phys. Rev. B **105**, 214402 (2022).

[37] F. Zheng, F. N. Rybakov, N. S. Kiselev, D. Song, A. Kovács, H. Du, S. Blügel, and R. E. Dunin-Borkowski, Magnetic skyrmion braids, Nat. Commun. **12**, 5316 (2021).

[38] M. Yan, R. Hertel, and C. M. Schneider, Calculations of three-dimensional magnetic normal modes in mesoscopic permalloy prisms with vortex structure, Phys. Rev. B **76**, 094407 (2007).

[39] J. Ding, G. N. Kakazei, X. Liu, K. Y. Guslienko, and A. O. Adeyeye, Higher order vortex gyrotropic modes in circular ferromagnetic nanodots, Sci. Rep. **4**, 4796 (2014).

[40] K. Guslienko, Magnetic vortex core string gyrotropic oscillations in thick cylindrical dots, Magnetism **2**, 239 (2022).

[41] S. Finizio, C. Donnelly, S. Mayr, A. Hrabec, and J. Raabe, Three-dimensional vortex gyration dynamics unraveled by time-resolved soft x-ray laminography with freely selectable excitation frequencies, Nano Lett. **22**, 1971 (2022).

[42] O. M. Volkov, D. Wolf, O. V. Pylypovskyi, A. Kákay, D. D. Sheka, B. Büchner, J. Fassbender, A. Lubk, and D. Makarov, Chirality coupling in topological magnetic textures with multiple magnetochiral parameters, Nat. Commun. **14**, 1491 (2023).

[43] M. Azhar, V. P. Kravchuk, and M. Garst, Screw dislocations in chiral magnets, Phys. Rev. Lett. **128**, 157204 (2022).

[44] S.-Z. Lin, J.-X. Zhu, and A. Saxena, Kelvin modes of a skyrmion line in chiral magnets and the associated magnon transport, Phys. Rev. B **99**, 140408(R) (2019).

[45] V. P. Kravchuk, U. K. Rößler, J. van den Brink, and M. Garst, Solitary wave excitations of skyrmion strings in chiral magnets, Phys. Rev. B **102**, 220408(R) (2020).

[46] N. M. Ryskin and D. I. Trubetskov, *Nonlinear Waves* (Nauka, Moscow, 2000).

[47] A. Nayfeh, *Perturbation Methods* (Wiley, New York, 2008).

[48] A. N. Bogdanov and D. A. Yablonskǐ, Thermodynamically stable "vortices" in magnetically ordered crystals. The mixed state of magnets, Zh. Eksp. Teor. Fiz. **95**, 178 (1989) [Sov. Phys. JETP **68**, 101 (1989)].

[49] A. Bogdanov and A. Hubert, Thermodynamically stable magnetic vortex states in magnetic crystals, J. Magn. Magn. Mater. **138**, 255 (1994).

[50] N. Papanicolaou and T. N. Tomaras, Dynamics of magnetic vortices, Nucl. Phys. B **360**, 425 (1991).

[51] A. A. Thiele, Steady–state motion of magnetic of magnetic domains, Phys. Rev. Lett. **30**, 230 (1973).

[52] C. Schütte and M. Garst, Magnon-skyrmion scattering in chiral magnets, Phys. Rev. B **90**, 094423 (2014).

[53] S.-Z. Lin, C. D. Batista, and A. Saxena, Internal modes of a skyrmion in the ferromagnetic state of chiral magnets, Phys. Rev. B **89**, 024415 (2014).

[54] M. J. Lighthill, Contributions to the theory of waves in nonlinear dispersive systems, IMA J. Appl. Math. **1**, 269 (1965).

[55] V. Zakharov and L. Ostrovsky, Modulation instability: The beginning, Physica D **238**, 540 (2009).

[56] Note that the nonlinear part of the dispersion relation (11a) comes with the negative sign.

[57] See Supplemental Material at http://link.aps.org/supplemental/10.1103/PhysRevB.108.144412 for movies describing propagation of the nonlinear waves, solitons, and breathers along the string.

[58] S. Komineas and N. Papanicolaou, Skyrmion dynamics in chiral ferromagnets, Phys. Rev. B **92**, 064412 (2015).

[59] V. P. Kravchuk, D. D. Sheka, U. K. Rößler, J. van den Brink, and Y. Gaididei, Spin eigenmodes of magnetic skyrmions and the problem of the effective skyrmion mass, Phys. Rev. B **97**, 064403 (2018).

[60] X. Wu and O. Tchernyshyov, How a skyrmion can appear both massive and massless, SciPost Phys. **12**, 159 (2022).

[61] F. G. Mertens, H. J. Schnitzer, and A. R. Bishop, Hierarchy of equations of motion for nonlinear coherent excitations applied to magnetic vortices, Phys. Rev. B **56**, 2510 (1997).

[62] R. Hertel and C. M. Schneider, Exchange explosions: Magnetization dynamics during vortex-antivortex annihilation, Phys. Rev. Lett. **97**, 177202 (2006).

[63] R. Hertel, S. Gliga, M. Fähnle, and C. M. Schneider, Ultrafast nanomagnetic toggle switching of vortex cores, Phys. Rev. Lett. **98**, 117201 (2007).

[64] A. S. Kovalev, F. G. Mertens, and H. J. Schnitzer, Cycloidal vortex motion in easy–plane ferromagnets due to interaction with spin waves, Eur. Phys. J. B **33**, 133 (2003).

[65] G. B. Whitham, A general approach to linear and non-linear dispersive waves using a lagrangian, J. Fluid Mech. **22**, 273 (1965).

[66] G. B. Whitham, *Linear and Nonlinear Waves* (Wiley, New York, 1999).

[67] V. I. Karpman and E. M. Krushkal, Modulated waves in nonlinear dispersive media, Zh. Eksp. Tear. Fiz. **55**, 530 (1968) [Sov. Phys. JETP **28**, 277 (1969)].

[68] V. I. Karpman, *Non-Linear Waves in Dispersive Media*, 1st ed. (Pergamon, 1975).

[69] V. E. Zakharov and S. A. B., Exact theory of two-dimensional self-focusing and one-dimensional self-modulation of waves in nonlinear media, Zh. Eksp. Teor. Fiz. **61**, 118 (1971) [Sov. Phys. JETP **34**, 62 (1972)].

[70] N. N. Akhmediev, V. M. Eleonskii, and N. E. Kulagin, Exact first-order solutions of the nonlinear schrödinger equation, Theor. Math. Phys. **72**, 809 (1987).

[71] K. B. Dysthe and K. Trulsen, Note on breather type solutions of the NLS as models for freak-waves, Phys. Scr. **1999**, 48 (1999).

[72] mumax3, developed by the DyNaMat group of Professor Van Waeyenberge at Ghent University.

[73] *NIST Handbook of Mathematical Functions*, edited by F. W. J. Olver, D. W. Lozier, R. F. Boisvert, and C. W. Clark (Cambridge University Press, New York, 2010).

[74] E. D. Skyllingstad, Critical layer effects on atmospheric solitary and cnoidal waves, J. Atmos. Sci. **48**, 1613 (1991).

[75] A. Vansteenkiste, J. Leliaert, M. Dvornik, M. Helsen, F. Garcia-Sanchez, and B. Van Waeyenberge, The design and verification of MuMax3, AIP Adv. **4**, 107133 (2014).

[76] Y.-C. Ma, The perturbed plane-wave solutions of the cubic schrödinger equation, Stud. Appl. Math. **60**, 43 (1979).

[77] D. H. Peregrine, Water waves, nonlinear schrödinger equations and their solutions, J. Aust. Math. Soc. Ser. B **25**, 16 (1983).

[78] B. F. McKeever, D. R. Rodrigues, D. Pinna, A. Abanov, J. Sinova, and K. Everschor-Sitte, Characterizing breathing dynamics of magnetic skyrmions and antiskyrmions within the hamiltonian formalism, Phys. Rev. B **99**, 054430 (2019).